Blackstart and Fault Ride-Through Capability of DFIG-Based Wind Turbines

Hoang P. Dang, *Student Member, IEEE* and Hugo N. Villegas Pico, *Member, IEEE*

***Abstract*—Grid-forming wind turbines must be able to re-energize transmission branches, motor loads, unbalanced loads, and power electronics loads following a blackout. Further, they must ride through faults that can arise during restoration. To tackle these challenges, this paper sets forth a grid-forming control strategy for wind turbines using doubly-fed induction generators (DFIGs). In particular, a special set of feedforward control loops are engineered to mitigate the impacts of restoration transients as well as symmetrical and asymmetrical faults on the regulation of DFIG rotor currents and stator voltages. This paper also leverages two-axis anti-windup regulators to bound two-axis voltage and current commands within ratings. The controller performance is demonstrated via a high-fidelity simulation model of a notional wind-dominant grid.**

***Index Terms*—Power generation reliability, power system restoration, wind power generation.**

I. Introduction

THE restoration of power grids in the United States of America (USA) solely relies on gas and hydro generating units [1]–[3]. However, this dependency contrasts the massive penetration of wind turbines in some states [4]. For example, 58% and 43% of the energy respectively consumed by Iowa and Kansas in year 2020 was generated by their 11-GW and 7-GW wind turbine fleets [4]. Hence, ascertaining whether wind turbines can support the recovery of wind-dominant power grids from blackouts is a timely resilience problem to study.

Gas and hydro power plants are attractive for blackstart and restoration because of their firm energy supply and electromechanical robustness to disturbances [2], [3]. Further, these classes of power plants have short startup times, steep ramp rates, and multiple generating units. In general, blackstart assets must be able to [1], [5]: (i) Self start when the grid is de-energized. (ii) Regulate voltage magnitudes and frequency. (iii) Energize power transformers, transmission lines, and loads. And (iv) Ride through symmetrical and asymmetrical faults.

Recently, the North American Electric Reliability Corporation (NERC) reported that the supply of natural-gas fuel can be at risk during extreme winter weather [6, p. 7] which impacts blackstart gas turbines. Impacts of cold weather on the natural gas transmission system has been reported in Rhode Island in 2019 [7] and in Texas in 2021 [8, p. 32]. Thus, hydro generators are the ideal blackstart assets [2]. Unfortunately, these resources are limited in west-north-central states of the USA which typically face relatively low temperature, e.g., -14°F [9], [10]. As a matter of fact, hydro resources generated less than 2% of the energy consumed in Iowa in 2020 [11].

TABLE I
Restoration Challenges Addressed by Select Controls

Ref.	[15]	[16]	[17]	[18]	[19]	[20]	[21]	[22]	[23]	[24]	[25]	[26]	[27]	[28]	[29]
(C1)	☑	☒	☒	☒	☒	☒	☒	☒	☒	☒	☑	☑	☑	☒	☑
(C2)	☒	☒	☒	☒	☒	☑	☒	☒	☒	☒	☒	☑	☒	☒	☒
(C3)	☑	☑	☑	☑	☑	☑	☒	☒	☒	☑	☒	☑	☒	☒	☒
(C4)	☒	☒	☒	☒	☒	☒	☒	☒	☒	☒	☒	☒	☒	☒	☒
(C5)	☒	☒	☒	☒	☒	☒	☒	☒	☒	☒	☒	☒	☒	☒	☒

An urgent need to secure blackstart resources in the north-west-central states of the USA emerged from the devastating derecho in August 2020 which caused a massive blackout [12]. Further, recent reports have determined the likelihood of blackouts and the reduction of blackstart assets [1], [3], [13]. Hence, it is strategic to purpose wind turbines, for example, as blackstart resources for grid recovery after a wind storm. Notably, Type 3 wind turbines, which use doubly-fed induction generators (DFIGs), respectively account for the 55.8% and 72.5% of the turbine fleet in Iowa and Kansas [14]. Present Type 3 turbines in the USA do not blackstart [1, p. 15].

In the literature, there exist control methods to blackstart Type 3 wind turbines [15]–[29]. As shown in Table I, there is no grid-forming technique that can meet *all* the following challenges. Wind turbines must [1], [5], [30]: (C1) Energize transmission lines which can cause over-voltages because of their capacitive nature. (C2) Power direct-drive motor loads which demand variable active and reactive power during rotor acceleration. (C3) Energize unbalanced and electronic loads which introduce negative-sequence components and nonlinear distortion. (C4) Ride through faults to not jeopardize a restoration process. And (C5) survive low wind speed events which can cause turbine stalling. Present wind, solar, and battery energy resources using phase-locked loops (PLLs) can address modern interconnection requirements [31]–[34]. However, they cannot restore power grids because their PLLs depend on externally generated voltages [35], [36].

In Table I, the most advanced grid-forming technique for Type 3 turbines can meet three out of five challenges by using rotor-flux oriented control [26]. Other ingenious techniques can handle unbalanced and nonlinear loads by using resonant proportional-integral (PI) controllers [17], fuzzy logic strategies [24], and negative-sequence compensation [19]. However,

This material is based upon work supported by the U.S. Department of Energy, Office of Science, Office of Basic Energy Sciences under Award Number DE-SC0021410 to Iowa State University. The views expressed in the article do not necessarily represent the views of the DOE or the U.S. Government. The U.S. Government retains and the publisher, by accepting the article for publication, acknowledges that the U.S. Government retains a nonexclusive, paid-up, irrevocable, worldwide license to publish or reproduce the published form of this work, or allow others to do so, for U.S. Government purposes.

H. P. Dang and H. N. Villegas Pico are with Iowa State University, Ames, IA 50011, USA (e-mail: {dhphuong, hvillega}@iastate.edu).

none of these control techniques are designed to withstand symmetrical and asymmetrical faults. Riding through faults is particularly difficult because it has not been conceived a current-limiting approach for Type 3 turbines so that they can maintain grid-forming operation while facing severe transients [15]–[29]. Synchronous machines can naturally maintain grid-forming operation during disturbances without current-limiting control because of their electromechanical nature [37]. In DFIG-based wind turbines, nonetheless, current-limiting is critical to not destroy the semiconductor switches of the rotor-side converters (RSCs) and grid-side converters (GSCs) [38].

Towards the reliable restoration of wind-dominant grids, this paper reports three contributions. (i) A procedure to blackstart and restore power grids using Type 3 turbines, q.v., Section II. The principle is to slightly raise the dc-link capacitor voltage using a small battery bank once the wind turbine is spinning. Then, the dc-link capacitor sparks the self-energization of the DFIG via the RSC and GSC without a battery. In present procedures, a battery bank is needed to *continuously* power the RSC during blackstart, q.v. [21], [24], [26]. (ii) A set of feedforward control loops to mitigate the impacts of restoration transients on grid-forming operation, q.v. Section III-B. To this end, this paper analyzes the relationship among DFIG stator and rotor currents as well as DFIG stator voltages and currents flowing into the grid to mitigate impacts on voltage regulation. This manuscript also leverages the feedforward voltages proposed in [33] to mitigate the development of DFIG rotor inrush currents from restoration transients. Present control loops do not incorporate feedforward currents because they are not designed for grid-forming operation during faults [15]–[29]. And (iii) a grid-forming control strategy that prevents the development of RSC and GSC over-currents during blackstart and faults, q.v. Sections III and IV. In Section III, this paper leverages a new class of two-axis anti-windup PI regulators to bound two-axis DFIG rotor current commands in a circle while stopping integration [30]. Present, control strategies do not employ current-limiters that can maintain grid-forming operation [15]–[29]. In Section IV, this paper proposes a method to synchronize the GSC to the DFIG stator voltages without using a PLL which is currently done, e.g., see [26]. A GSC control strategy is also engineered to ride through faults via anti-windup PI loops.

These contributions are demonstrated in a detailed simulation model that includes: three Type 3 turbines, twelve circuit breakers, two transmission cables, two direct-drive motors, one unbalanced load, one power-electronics load, and a line-to-line fault. Engineering a grid-forming controller for Type 3 turbines is more challenging than for Type 4 units [30] because the DFIG is directly exposed to restoration transients.

This paper is timely to engineer wind-dominant grids that are resilient to blackouts and reliable to faults [39]. Further, this paper is useful to: (i) satisfy NERC standards EOP-005-3 [40] and PRC-024-3 [34], (ii) secure blackstart resources for local reliability and resilience [41, p. 4], and (iii) address the third grand challenge of wind energy [42]. This grand challenge refers to the ability of wind turbines to withstand electromagnetic disturbances and to autonomously regulate frequency and voltages while supplying the demand.

The remaining of the exposition is presented as follows. Section II succinctly introduces about blackstart and restoration processes as well as preliminary information for control. Sections III and IV detail the functionalities of the grid-forming controller for blackstart and restoration. Section V contains two case studies that highlights the proposed advances in a notional wind-dominant grid. Section VI concludes.

II. Blackstart and Restoration Processes

We illustrate in Fig. 1 the classical topology of a Type 3 wind turbine which is explained in [38, p. 68]. In typical Type 3 turbines, the RSC is used to regulate aerodynamic power extraction [38] whereas the GSC is used to regulate dc-link voltage. The blade pitch angle is used to limit aerodynamic power extraction. During a blackout, typical control loops cannot operate because they resort to PLLs which in turn require of an energized grid for angle tracking.

In this paper, the RSC is used to regulate DFIG stator voltages. In lieu of a PLL, the control loops depend on a speed-droop control law [43] for autonomous operation from synchronous machines. On the other hand, the blade pitch angle is used for active control of DFIG rotor speed. The objective of the GSC does not change with respect to its typical function [38]. The dc-link braking resistor (BKR) in Fig. 1 is still necessary to ride through faults. The proposed controller in Fig. 2 serves to restore the notional wind-dominant grid in Fig. 3. The variables in Figs. 1–3 are defined in Table II.

The novelty of this section is a blackstart procedure that depends on a slightly pre-charged dc-link capacitor by *momentarily* using a boost converter (BTC) and a small battery bank, q.v. Fig. 1. Present schemes to blackstart Type 3 turbines use a battery bank to *sustain* the operation of the RSC throughout the startup process, e.g., see [21], [24], [26]. Hence, the GSC has not been leveraged to self-energize and sustain ac and dc voltages of Type 3 turbines during blackstart. The proposed idea is inspired by field-flashing procedures for self-excited synchronous machines via a small battery [44]. This section is also salient because it fuses NERC standards within the blackstart and restoration description [34], [40].

A. Blackstart Process

Before initiating a blackstart process, this paper assumes: (i) the wind turbine is isolated from the grid, (ii) the RSC and GSC controllers are turned off, (iii) the speed of the DFIG rotor ω_m has reached its set-point ω_m^*, and (iv) the value of the dc-link capacitor voltage is relatively small, e.g., 5% of rated. Here, ω_m^* is 30% above rated speed to store maximum kinetic energy for cold load pick-up.[1] A small battery bank is necessary to power speed control processes and slightly pre-charge the dc-link capacitor [3], [30]. In this paper, the BTC in Fig. 1 is used to raise the dc-link voltage from $0.0\,\text{kV}$ to $0.1\,\text{kV}$ which is 5% of rated, i.e., $v_{dc}^\star = 2\,\text{kV}$. Thus, the battery sources $0.5 \cdot C \cdot (0.05 v_{dc}^\star)^2 = 250\,\text{J}$ or $0.07\,\text{Wh}$ for $C = 50\,\text{mF}$ which is negligible. Afterwards, the BTC isolates the battery from the blackstart process.

[1] Wind turbines are designed to operate within $\pm 30\,\%$ from rated speed [38].

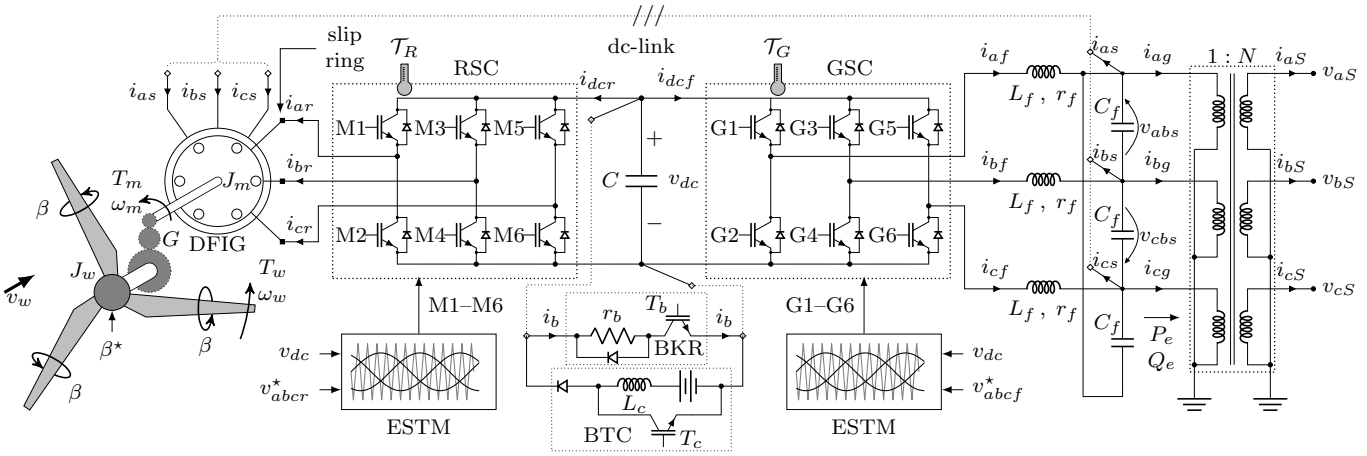

Fig. 1. Type 3 wind turbine drive system displaying a braking resistor (BKR) and a boost converter (BTC) for dc-link voltage control.

TABLE II
DESCRIPTION OF PHYSICAL AND ABSTRACT VARIABLES

(*abc*) variables	*qd* variables	Description
i_{as}, i_{bs}, i_{cs}	i^{e}_{qs}, i^{e}_{ds}	DFIG stator currents
i_{ar}, i_{br}, i_{cr}	i'^{s}_{qr}, i'^{s}_{dr}	DFIG rotor currents
i_{af}, i_{bf}, i_{cf}	$i^{\mathsf{e/c}}_{qf}$, $i^{\mathsf{e/c}}_{df}$	GSC inductor currents
i_{ag}, i_{bg}, i_{cg}	i^{e}_{qg}, i^{e}_{dg}	transformer/grid currents
v_{abs}, v_{cbs}	$v^{\mathsf{e/c}}_{qs}$, $v^{\mathsf{e/c}}_{ds}$	line-to-line capacitor/stator voltages
v_{abS}, v_{cbS}	v^{e}_{qS}, v^{e}_{dS}	line-to-line PCC voltages
v_{abR}, v_{cbR}	v^{e}_{qR}, v^{e}_{dR}	line-to-line load feeder voltages
$v^{\star}_{ar}$, $v^{\star}_{br}$, $v^{\star}_{cr}$	$v'^{\star}_{qr}$, $v'^{\star}_{dr}$	RSC ESTM commands
$v^{\star}_{af}$, $v^{\star}_{bf}$, $v^{\star}_{cf}$	$v^{\star}_{qf}$, $v^{\star}_{df}$	GSC ESTM commands
C,v_{dc}	-	dc-link capacitance and voltage
r_b, i_b	-	BKR resistance and current
L_f, r_f, C_f	-	filter inductance, resistance, capacitance
ω_m, θ_m	-	DFIG angular speed and rotor position
T_m, T_e	-	DFIG mech. and electromagn. torques
β, v_w	-	blade pitch angle and wind speed
T_w, ω_w	-	aerodynamic torque and turbine speed
G	-	turbine gearbox ratio
J_m, J_w	-	DFIG and wind turbine inertia
$\mathcal{T}_R$,$\mathcal{T}_G$	-	RSC and GSC junction temperature
P_e, Q_e	-	DFIG active and reactive power output
P_M	-	active power by the motor load
P_Z	-	active power by the unbalanced load
P_E	-	active power by the electronic load
i_{aF}, i_{bF}, i_{cF}	-	fault currents

To blackstart the turbine in Fig. 1, the RSC controller is turned on to build up stator voltages which further charges the dc-link capacitor because the off GSC acts as a full-wave rectifier, q.v. the GSC anti-parallel diodes in Fig. 1. More precisely, the goal of the RSC controller is to regulate line-to-line stator voltages v_{abs} and v_{cbs}, q.v. Fig. 1, so that their voltage magnitude V_s follows the reference $V_s^\star$ while cycling at synchronous speed ω_{e}. To that end, the RSC controller outputs the control commands $v^\star_{abcr} = [v^\star_{ar}, v^\star_{br}, v^\star_{cr}]^\top$ which drive an extended sine triangle modulator (ESTM).

Then, the GSC controller is turned on to regulate the dc-link voltage so that v_{dc} reaches $v^\star_{dc}$ by steering $v^\star_{abcf} = [v^\star_{af}, v^\star_{bf}, v^\star_{cf}]^\top$. The DFIG speed controller in Fig. 2 commands a servo-system to steer β towards the set-point $\beta^\star$ to maintain ω_m at ω^*_m during variation of wind speed. The command $\overline{P}_e$ from the speed controller informs the RSC controller in Fig. 2 about the available aerodynamic power that can be transferred to the grid [30]. Once each wind turbine of Fig. 3 has started up, they are synchronized at the point of common coupling (PCC) by closing C1–C3. Now, the power plant is ready for restoration.

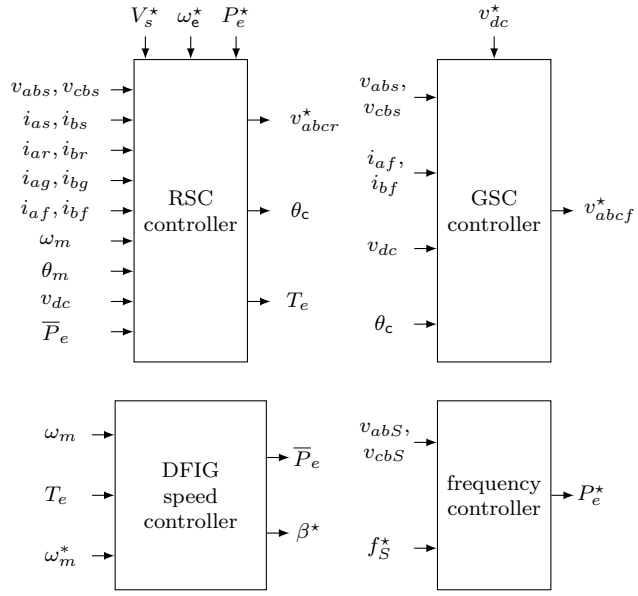

Fig. 2. Grid-forming and power plant frequency controllers.

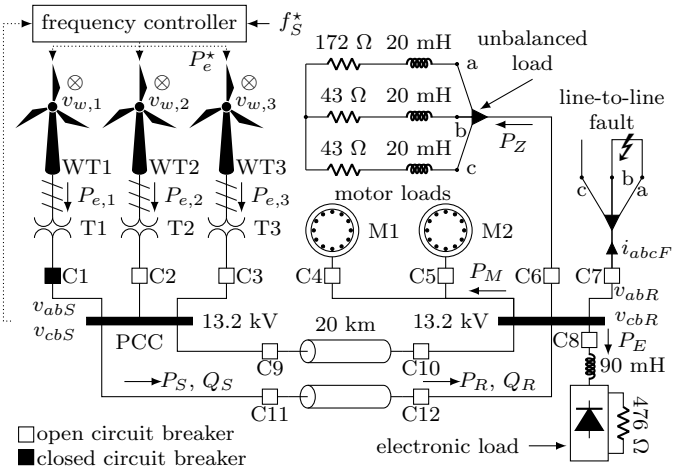

Fig. 3. Notional wind-dominant power system with Type 3 wind turbines.

B. Restoration Process

A restoration process is a sequence of planned steps to supply electricity to consumers after a blackout. NERC stan-

dard EOP-005-3 ensures that facilities, plans, and personnel are prepared to enable system restoration from blackstart resources [40]. The first goal of a restoration plan is to energize a cranking or transmission path to energize auxiliary systems of next-start generating stations, e.g., thermal power plants. In Fig. 3, the transmission path is represented with two 20-km cables and the auxiliary systems are modeled with direct-drive motor loads. The second goal is to energize consumer loads which are sometimes instrumental to stabilize system voltages during recovery [1]. The unbalanced and electronic loads in Fig. 3 are representative of electricity demand by consumers. Unbalanced and electronic loads are considered because they challenge control of DFIG wind turbines [17]. Restoration is conducted by closing circuit breakers to form a path between the blackstart resources and the next-start units or loads [1]. In Fig. 3, there are twelve circuit breakers, viz., C1–C12, that are involved in the restoration process.

During load pick-up, frequency can deviate from rated because of the considered speed-droop control law for grid-forming operation [43]. Hence, a power plant frequency controller in Fig. 2 is needed to maintain frequency, f_S, at the set-point, $f_S^\star$ [30]. Here, f_S is estimated using a phase-locked loop that uses line-to-line voltage waveforms at the PCC, q.v. Fig. 3. The frequency controller generates a common power command, $P_e^\star$, that are passed to each wind turbine RSC controller in Fig. 2, q.v. [30].

During restoration, an operator of the hypothetical grid in Fig. 3 might inadvertently switch onto an asymmetrical fault when closing circuit breaker C7, for example. Notably, some power companies simulate faults during restoration to assess the ability of blackstart resources to ride through faults to not jeopardize restoration [1, p. 30]. Thus, it is important to ascertain whether grid-forming Type 3 turbines can ride through faults to satisfy NERC reliability standard PRC-024-3 [34]. In this paper, we monitor IGBT junction temperature of the RSC, $\mathcal{T}_R$, to ensure it is not damaged during severe faults. The dc braking resistor (BKR) in Fig. 1 serves to prevent deleterious high dc voltage during disturbances [45].

C. Transformation of Variables

In this paper, the RSC, GSC, and frequency controllers in Fig. 2 are synthesized using abstract *qd* variables which are calculated from *abc* quantities as reported in the Appendix. To that end, we use the angles of three reference frames:

$$\frac{d}{dt}\theta_\nu = \omega_\nu \tag{1}$$

with $\nu \in \{\mathsf{e}, \mathsf{s}, \mathsf{c}\}$ to respectively map *abc* stator, rotor, and GSC variables into *qd* ones. In particular, θ_e is from a speed-droop control law, $\theta_\mathsf{s} = \theta_\mathsf{e} - \theta_\mathsf{r}$ with θ_r the DFIG electrical rotor position [46, Ch. 5], and θ_c is calculated from DFIG-stator voltages in the 'e' reference frame.

To simplify notation of *qd*-variables in a ν frame, we define:

$$f^\nu_{qdx} \triangleq [f^\nu_{qx}, f^\nu_{dx}]^\top \text{ and } f^\nu_{dqx} \triangleq [f^\nu_{dx}, -f^\nu_{qx}]^\top \tag{2}$$

where $f \in \{v, i, \lambda\}$ can represent voltage, current or flux linkage. Further, $x \in \{r, s, f, g, S, R\}$ respectively represents quantities related to the DFIG rotor, DFIG stator, GSC filter, step-up transformer, PCC, and load feeder. For example, v^e_{qds} in Table II are obtained from v_{abs} and v_{cbs} in Fig. 1 within the RSC controller of Fig. 2 using $\theta_\nu = \theta_\mathsf{e}$ which is in (4). Similarly, i^e_{qdg} are from i_{ag} and i_{bg} in Fig. 1 within the RSC controller using (50) when $\theta_\nu = \theta_\mathsf{e}$ from (4), q.v., the Appendix.

For reporting purposes, the per-unit magnitude of f^ν_{qdx} is:

$$\breve{F}_x = F_x / F_{bx} \text{ with } F_x = \sqrt{(f^\nu_{qx})^2 + (f^\nu_{dx})^2}\,. \tag{3}$$

with F_{bx} a base constant.

D. Reference Frame Angles

For the grid-forming operation of the RSC and GSC controllers, the angles of the 'e' and 'c' frames are critical. These angles are autonomously synthesized within the wind turbine controllers to not depend on PLLs. The 'e' frame angle:

$$\frac{d}{dt}\theta_\mathsf{e} = \omega_\mathsf{e} \text{ with } \theta_\mathsf{e}(t^+) = \begin{cases} \theta_\mathsf{e}(t) & \text{if } 0 \le \theta_\mathsf{e}(t) < 2\pi \\ 0 & \text{if } \theta_\mathsf{e}(t) = 2\pi \end{cases} \tag{4}$$

whereas the speed of this 'e' frame meets [30], [43]:

$$\omega_\mathsf{e} = \omega^\star_\mathsf{e} + \frac{\omega_b}{P_{e,\text{mx}}} k_\omega (P^*_e - \widetilde{P}_e) - \omega_a \omega_b\,. \tag{5}$$

Note here that ω_e can also be implemented to emulate the inertial dynamics of the rotor of a synchronous machine [26].

The innovation term ω_a in (5) with respect to [43] serves to survive low wind speed events [30]. In (5), k_ω is the speed-droop constant, P^*_e is a power set-point, ω_b is a base angular frequency, $P_{e,\text{mx}}$ is rated electric power. The filtered electric power, $\widetilde{P}_e$, into the grid as shown in Fig. 1 is:

$$\frac{d}{dt}\widetilde{P}_e = \frac{1}{\tau_e}(-\widetilde{P}_e + P_e)\ ,\ \ P_e = \frac{3}{2}(v^\mathsf{e}_{qs} i^\mathsf{e}_{dg} + v^\mathsf{e}_{ds} i^\mathsf{e}_{qg})\,. \tag{6}$$

The angle of the 'c' frame is used to synchronize the GSC variables with DFIG stator voltages and is calculated with [46]:

$$\theta_\mathsf{c} = \texttt{angle}\,(v_{\alpha\beta s}) \tag{7}$$

$$\begin{bmatrix} v_{\alpha s} \\ v_{\beta s} \end{bmatrix} = \begin{bmatrix} \cos(\theta_\mathsf{e}) & \sin(\theta_\mathsf{e}) \\ \sin(\theta_\mathsf{e}) & -\cos(\theta_\mathsf{e}) \end{bmatrix} \begin{bmatrix} \overline{v}_{qs} \\ \overline{v}_{ds} \end{bmatrix} \tag{8}$$

$$\frac{d}{dt}\overline{v}_{qds} = \frac{1}{\tau_v}(-\overline{v}_{qds} + v^\mathsf{e}_{qds}) \tag{9}$$

because θ_e and v^e_{qds} are available, q.v. Fig. 2. The operator $\texttt{angle}(\cdot)$ returns the angle of $v_{\alpha\beta s} = [v_{\alpha s}, v_{\beta s}]^\top$. A low-pass filter with time constant τ_v is used in (9) [and (19)] to filter double frequency oscillations and nonlinear distortion from unbalanced and electronic loads.

III. Rotor Side Converter Controller

For voltage regulation, the RSC of Fig. 1 is controlled using: (i) feedforward control loops to mitigate restoration transients and (ii) two-axis anti-windup PI regulators to bound *qd* control quantities in a circle which are significant novelties in this paper. The strength of the controller is its ability to withstand restoration transients and ride through symmetrical and asymmetrical faults, q.v. Section V. Control of DFIG stator voltage is achieved by driving DFIG rotor currents using intuition from control of synchronous machines.

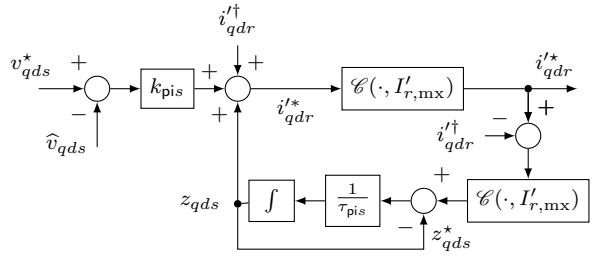

(a) DFIG-stator voltage regulator

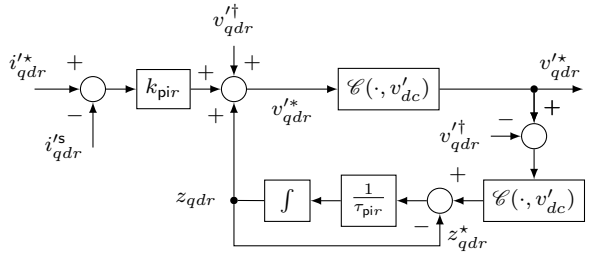

(b) RSC current regulator

Fig. 4. RSC voltage and current regulators using two-axis anti-windup PI regulators that bound the *qd* integrators and control commands in a circle.

A. Stator Voltage Controller

Regulation of DFIG stator voltages for grid-forming operation is achieved by regulating *qd* rotor currents, i'^{s}_{qdr}.[2] One novelty is that stator voltages are regulated via the two-axis anti-windup PI controller depicted in Fig. 4a which satisfies:

$$i'^{*}_{qdr} = k_{\mathsf{pis}}(v^\star_{qds} - \widehat{v}_{qds}) + z_{qds} + i'^{\dagger}_{qdr} \tag{10}$$

$$i'^{\star}_{qdr} = \mathscr{C}(i'^{*}_{qdr}, I'_{r,\mathrm{mx}}) \tag{11}$$

$$\frac{d}{dt} z_{qds} = \frac{1}{\tau_{\mathsf{pis}}}(-z_{qds} + z^\star_{qds}) \tag{12}$$

$$z^\star_{qds} = \mathscr{C}(i'^{\star}_{qdr} - i'^{\dagger}_{qdr}, I'_{r,\mathrm{mx}}) \tag{13}$$

with $I'_{r,\mathrm{mx}} = N_{rs} I_{r,\mathrm{mx}}$. Here, $I_{r,\mathrm{mx}}$ is rated peak rotor current and N_{rs} is the rotor-to-stator turn ratio. The RSC current commands $i'^{\star}_{qdr}$ in (11) are the set-points for the RSC current controller which drive i'^{s}_{qdr} in Fig. 4b. The feedforward currents, $i'^{\dagger}_{qdr}$, in (10) and (13) mitigate the impacts of restoration transients and faults, q.v. Section III-B.

The *qd* set-points for the voltage regulator in (10) are:

$$v^\star_{qds} = \sqrt{\frac{2}{3}} v_V v_\omega \left[V^\star_s, 0\right]^\top \tag{14}$$

Here, $V^\star_s$ is the line-to-line rms voltage set-point and:

$$v_V = 1 - k_V \frac{\widetilde{i}^{\mathsf{c}}_{dg}}{I_{s,\mathrm{mx}}} \text{ and } v_\omega = \min\left\{1, \frac{\omega_{\mathsf{e}}}{\omega_b} k_{\mathrm{V/Hz}}\right\} \tag{15}$$

are voltage droop and volts-per-hertz functionalities, respectively. The parameters k_V and $k_{\mathrm{V/Hz}}$ are respectively per-unit voltage droop constant and per unit volts-per-hertz limit, which is 1.05 p.u. in the USA [47]. The parameter, $I_{s,\mathrm{mx}}$, is stator rated peak current. The volts-per-hertz functionality serves to automatically adjust $v^\star_{qds}$ if the synchronous speed ω_{e} in (5) drops during low wind speed events [30] as to prevent electric machinery from over-fluxing [47].

[2]We use 'primes' to signify that rotor variables are referred to the stator.

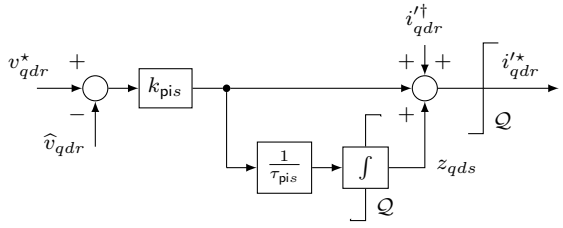

(a) Stator voltage controller using two independent PI regulators.

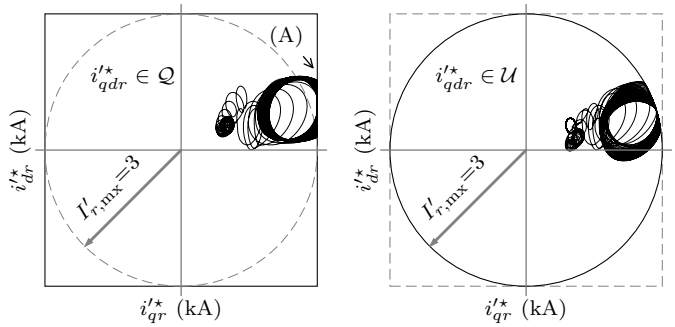

(b) Two independent PI regulators (c) Two-axis anti-windup regulators

Fig. 5. RSC *qd* currents commands generated by two classes of anti-windup PI regulators during a line-to-line fault.

In (11) and (13), the function $\mathscr{C} : \mathbb{R}^2 \times \mathbb{R}_+ \mapsto \mathbb{R}^2$ such that:

$$\mathscr{C}(u^*_{qd}, U_{\mathrm{mx}}) = \begin{cases} \frac{U_{\mathrm{mx}}}{U} u^*_{qd} & \text{if } U > U_{\mathrm{mx}} \neq 0 \\ u^*_{qd} & \text{otherwise} \end{cases} \tag{16}$$

$$U = \sqrt{u^{*2}_q + u^{*2}_d} \tag{17}$$

is used to bound the integrator states z_{qds} and current commands $i'^{\star}_{qdr}$ in an origin-centered circle $\mathcal{U}$ of radius $I'_{r,\mathrm{mx}}$. For voltage droop in (15), consider the filtered version of i^{c}_{dg}:

$$\frac{d}{dt}\widetilde{i}^{\mathsf{c}}_{dg} = \frac{1}{\tau_g}(-\widetilde{i}^{\mathsf{c}}_{dg} + i^{\mathsf{c}}_{dg})\,. \tag{18}$$

Note here that the proposed voltage controller in Fig. 4a contrasts the classical one in Fig. 5a which uses two independent *qd* anti-windup regulators. A problem with the approach in Fig. 5a is that it bounds z_{qds} and $i'^{\star}_{qdr}$ quantities in a origin-centered/axis-aligned square $\mathcal{Q}$ which can cause the violation of RSC rated currents, i.e., $I'_{r,\mathrm{mx}}$, during faults. Figure 5 respectively illustrates violation and compliance of rated *qd* rotor commands, $i'^{\star}_{qdr}$, when bounding control signals in an square, $\mathcal{Q}$, and in a circle, $\mathcal{U}$, during the line-to-line fault event that is studied in Section V. In Fig. 5b, the label (A) shows violation of $\mathcal{U}$ with radius 3.0 kA when current commands are bounded by $\mathcal{Q}$. Note that IEEE 2800 specifies that currents of converter-based generation may remain bounded in an origin-centered circle [48, pp. 12–21].

In (10), the sensed stator voltages $\widehat{v}_{qds} = [\widehat{v}_{qs}, \widehat{v}_{ds}]^\top$ are:

$$\frac{d}{dt}\widehat{v}_{qs} = \frac{1}{\tau_v}\left(-\widehat{v}_{qs} + V_s\right),\ \widehat{v}_{ds} = 0 \tag{19}$$

$$V_s = \sqrt{(v^{\mathsf{e}}_{qs})^2 + (v^{\mathsf{e}}_{ds})^2} \tag{20}$$

to stimulate only $i'^{\star}_{qr} \geq 0$ for regulation of stator voltages as done in synchronous generators. We recall that voltage in synchronous machines is regulated by steering the field winding or one-axis current only. In our control approach, the

current command, $i'^{\star}_{dr}$, can freely develop, nonetheless, $i'^{\star}_{qdr}$ from (11) always belong to a circle of radius $I'_{r,\mathrm{mx}}$.

B. RSC Feedforward Currents

Another novelty of this paper is the calculation of the *qd* feedforward currents, $i'^{\dagger}_{qdr}$, for (10) and (13). These currents have not been devised in the grid-forming literature [15]–[29]. For example, the grid-forming strategy in [26] does not employ feedforward terms because DFIG stator voltages are controlled by regulating abstract fluxes which are steered via proportional control. However, this approach is not suitable to limit RSC currents during faults and causes significant voltage drop during motor startup. In this paper, the purpose of $i'^{\dagger}_{qdr}$ is to mitigate the impacts of a variety of electrical transients on *qd* stator voltages which satisfy [46]:

$$3C_f \frac{d}{dt} v^{\mathsf{e}}_{qds} = i^{\mathsf{e}}_{qdf} - i^{\mathsf{e}}_{qdg} - i^{\mathsf{e}}_{qds} - 3C_f \omega_{\mathsf{e}} v^{\mathsf{e}}_{dqs} \tag{21}$$

because there is a delta-connected capacitor bank in the DFIG stator, q.v. Fig. 1. Equation (21) is formulated from the application of *qd* Kirchhoff's current law at the *qd* nodes where the currents from the DFIG stator, GSC filter, ac capacitor, and the low voltage side of the step-up transformer meet, q.v. Fig. 1.

A challenging task is to devise from (21) an expression for $i'^{\dagger}_{qdr}$ in (10) and (13) to mitigate impacts of severe restoration transients on v^{e}_{qds} by steering $i'^{\star}_{qdr}$.

Proposition 1: The feedforward currents, $i'^{\dagger}_{qdr}$, satisfying:

$$\frac{L_M}{L_{ss}} i'^{\dagger}_{qdr} = -\widetilde{i}^{\mathsf{e}}_{qdf} + \widetilde{i}^{\mathsf{e}}_{qdg} - \left(\frac{1}{\omega_{\mathsf{e}} L_{ss}} - 3C_f \omega_{\mathsf{e}} \right) \widetilde{v}^{\mathsf{e}}_{dqs} \tag{22}$$

mitigate the impacts of DFIG stator currents, GSC filter currents, transformer currents from the grid, and speed currents on *qd* stator voltages.

Proof: Consider quasi-steady state DFIG stator and rotor currents by neglecting DFIG resistances. Thus, stator currents as function of *qd* stator voltages and rotor currents are:

$$i^{\mathsf{e}}_{qds} \approx -\frac{1}{\omega_{\mathsf{e}} L_{ss}} v^{\mathsf{e}}_{dqs} - \frac{L_M}{L_{ss}} i'^{\mathsf{s}}_{qdr} \tag{23}$$

from [46, Ch. 6] where $L_{ss} = L_{ls} + L_M$, q.v. Table III. Substitution of (23) into (21) yields:

$$3C_f \frac{d}{dt} v^{\mathsf{e}}_{qds} \approx i^{\mathsf{e}}_{qdf} - i^{\mathsf{e}}_{qdg} + \left(\frac{1}{\omega_{\mathsf{e}} L_{ss}} - 3C_f \omega_{\mathsf{e}} \right) v^{\mathsf{e}}_{dqs} + \frac{L_M}{L_{ss}} i'^{\mathsf{s}}_{qdr} \,. \tag{24}$$

implying (22) when $i'^{\mathsf{s}}_{qdr} = i'^{\dagger}_{qdr}$ so that $dv^{\mathsf{e}}_{qds}/dt = [0,0]^{\top}$ for cancellation of disturbance impacts on v^{e}_{qds}. The tildes in (22) signify filtered versions of v^{e}_{dqs}, i^{e}_{qdg}, and i^{e}_{qdf} via:

$$\frac{d}{dt} \widetilde{v}^{\mathsf{e}}_{dqs} = \frac{1}{\tau_s} (-\widetilde{v}^{\mathsf{e}}_{dqs} + v^{\mathsf{e}}_{dqs}) \,, \tag{25}$$

$$\frac{d}{dt} \widetilde{i}^{\mathsf{e}}_{qdg} = \frac{1}{\tau_s} (-\widetilde{i}^{\mathsf{e}}_{qdg} + i^{\mathsf{e}}_{qdg}) \text{ and } \frac{d}{dt} \widetilde{i}^{\mathsf{e}}_{qdf} = \frac{1}{\tau_s} (-\widetilde{i}^{\mathsf{e}}_{qdf} + i^{\mathsf{e}}_{qdf}) \,. \tag{26}$$

Filtering is necessary to mitigate the impacts of unbalanced and nonlinear loads on voltage regulation. ■

C. RSC Current Controller

Here, feedforward voltages are introduced to mitigate the impacts from stator currents and the cross coupling of *qd* rotor currents on regulation of rotor currents. The goal is to prevent the RSC from over-currents during restoration transients and faults. To this end, the RSC ESTM *qd* commands, $v'^{\star}_{qdr}$, originate from the following anti-windup PI regulator:

$$v'^{*}_{qdr} = k_{\mathsf{pir}} (i'^{\star}_{qdr} - i'^{\mathsf{s}}_{qdr}) + z_{qdr} + v'^{\dagger}_{qdr} \tag{27}$$

$$v'^{\star}_{qdr} = \mathscr{C} \left(v'^{*}_{qdr}, v'_{dc} \right) \text{ with } v'_{dc} = v_{dc}/(\sqrt{3} N_{rs}) \tag{28}$$

$$\frac{d}{dt} z_{qdr} = \frac{1}{\tau_{\mathsf{pir}}} (-z_{qdr} + z^{\star}_{qdr}) \tag{29}$$

$$z^{\star}_{qdr} = \mathscr{C} \left(v'^{\star}_{qdr} - v'^{\dagger}_{qdr}, v'_{dc} \right) \tag{30}$$

which is illustrated in Fig. 4b. Here, $i'^{\star}_{qdr}$ are from (11), $\mathscr{C}(\cdot,\cdot)$ is from (16), and $v'^{\dagger}_{qdr}$ are the feedforward voltages [33]:

$$v'^{\dagger}_{qdr} = -\frac{L_M}{L_{ss}} r_s i^{\mathsf{e}}_{qds} - \omega_{\mathsf{r}} L_M i^{\mathsf{e}}_{dqs} + \left(\omega_{\mathsf{e}} \frac{D}{L_{ss}} - \omega_{\mathsf{r}} L'_{rr} \right) i'^{\mathsf{s}}_{dqr} \tag{31}$$

where $D = L_{ss} L'_{rr} - L^2_M$ [46, p. 229]. The stator voltages v^{e}_{qds} used in [33] do not appear in (31) because they are no longer external disturbances, but controlled variables. The *qd* voltage set-points $v'^{\star}_{qdr}$ in (28) are used to generate the RSC ESTM commands $v^{\star}_{abcr} = N_{rs} T^{\top}(\theta_{\mathsf{s}}) v'^{\star}_{qdr}$ that drive the RSC in Fig. 1. Please, refer to the Appendix for details about $T(\theta_{\mathsf{s}})$.

IV. Grid Side Converter Controller

This section specifies the GSC controller to regulate dc-link voltage and to support DFIG stator voltage regulation. The novelties are methods for GSC synchronization with DFIG-stator voltages and fault ride-through capability. Present grid-forming strategies use a PLL for GSC synchronization and do not consider two-axis current-limiters, e.g., see [15]–[29].

A. GSC and DFIG Synchronization

The main challenge for GSC control is that the angle of the 'e' frame, θ_{e}, in (4) does not produce $v^{\mathsf{e}}_{ds} = 0$ in quasi-steady state because $i'^{\star}_{dr}$ from (11) is not used to steer $v^{\mathsf{e}}_{ds} \to 0$. Please, recall that the objective of the voltage controller in Section III-A is to regulate voltage magnitude as done in synchronous machines by controlling the field or one-axis current [37, Ch. 4]. Hence, $i'^{\star}_{qr}$ is only employed for voltage regulation. To synchronize the GSC to the DFIG stator voltage, this paper considers the reference frame angle θ_{c} in (7) based on v^{e}_{qds}, q.v. Table II. Hence, a PLL is not necessary to generate the angle of a reference frame for GSC control purposes. In the 'c' reference frame, $v^{\mathsf{c}}_{ds} = 0$ which is useful to regulate i^{c}_{qf} and i^{c}_{df} for dc-link voltage control and stator voltage support, respectively.

B. GSC Current Controller

The GSC regulates dc-link voltage and support DFIG stator voltages by controlling GSC currents i^{c}_{qdf}. To this end, this paper defines $v^{\star}_{abcf} = T^{\top}(\theta_{\mathsf{c}}) v^{\star}_{qdf}$ which drive the GSC ESTM

in Fig. 1. Please, refer to the Appendix for further details about $T(\theta_{\mathsf{c}})$. Specifically, the *qd* commands $v^{\star}_{qdf}$ are from the following two-axis anti-windup PI regulator:

$$v^{*}_{qdf} = k_{\mathsf{pi}f}(i^{\star}_{qdf} - i^{\mathsf{c}}_{qdf}) + z_{qdf} + v^{\dagger}_{qdf} \tag{32}$$

$$v^{\star}_{qdf} = \mathscr{C}\ (v^{*}_{qdf}, v_{dc}/\sqrt{3}) \tag{33}$$

$$\frac{d}{dt}z_{qdf} = \frac{1}{\tau_{\mathsf{pi}f}}(-z_{qdf} + z^{\star}_{qdf}) \tag{34}$$

$$z^{\star}_{qdf} = \mathscr{C}\ (v^{\star}_{qdf} - v^{\dagger}_{qdf}, v_{dc}/\sqrt{3}) \tag{35}$$

$$v^{\dagger}_{qdf} = \omega_{\mathsf{e}} L_f i^{\mathsf{c}}_{dqf} + v^{\mathsf{c}}_{qds}\,. \tag{36}$$

The saturation function $\mathscr{C}(\cdot,\cdot)$ is defined in (16). The feedforward voltages $v^{\dagger}_{qdf}$ mitigate impacts of restoration transients on GSC current regulation. The novelty of (32)–(35) is that they bound v^{*}_{qdf} within a circle of radius $v_{dc}/\sqrt{3}$ to prevent the integrator state z_{qdf} from winding up because [46, Ch. 12]:

$$\left(v^{*}_{qf}\right)^2 + \left(v^{*}_{df}\right)^2 < \left(\frac{v_{dc}}{\sqrt{3}}\right)^2 \tag{37}$$

models the limitation of v_{dc} to synthesize v^{*}_{qdf} with the GSC.

C. Dc-Link Voltage Controller

The strategy is to control dc-link voltage v_{dc} in Fig. 1 by regulating the energy stored in the dc-link capacitor $E_{dc} = (C/2)\,(v_{dc})^2$ so that it follows $E^{\star}_{dc} = (C/2)\,(v^{\star}_{dc})^2$, q.v. Fig. 1. To this end, the command $i^{\star}_{qf}$ for (32) is steered using a one-axis anti-windup PI regulator [49, p. 91]:

$$i^{*}_{qf} = k_{\mathsf{pi}c}(E_{dc} - \widetilde{E}^{\star}_{dc}) + z_{qe} \tag{38}$$

$$\frac{d}{dt}z_{qe} = \frac{1}{\tau_{\mathsf{pi}c}}(-z_{qe} + i^{\star}_{qf}) \tag{39}$$

$$i^{\star}_{qf} = \mathscr{L}\left(i^{*}_{qf}, -I_{f,\mathrm{mx}}, I_{f,\mathrm{mx}}\right) \tag{40}$$

to not violate the GSC current rating $I_{f,\mathrm{mx}}$. The voltage v_{dc} is not directly controlled to avoid handling nonlinear dynamics. In (40), $I_{f,\mathrm{mx}}$ is the rated GSC peak current. During the fault, the dc-link voltage can rise, hence, the BKR of Fig. 1 can activate to protect the RSC and GSC semiconductor switches.

In (38), the command $\widetilde{E}^{\star}_{dc}$ is obtained from:

$$\frac{d}{dt}\widetilde{E}^{\star}_{dc} = \frac{1}{\tau_E}(-\widetilde{E}^{\star}_{dc} + E^{\star}_{dc})\,. \tag{41}$$

to gradually build-up dc-link voltage during startup [50, p. 51]. In (40), $\mathscr{L} : \mathbb{R}\times\mathbb{R}\times\mathbb{R} \mapsto [u_{\mathrm{mn}}, u_{\mathrm{mx}}]$ ($u_{\mathrm{mn}} \le u_{\mathrm{mx}}$) such that:

$$\mathscr{L}(u, u_{\mathrm{mn}}, u_{\mathrm{mx}}) = \begin{cases} u_{\mathrm{mx}} & \text{if } u > u_{\mathrm{mx}} \\ u_{\mathrm{mn}} & \text{if } u < u_{\mathrm{mn}} \\ u & \text{otherwise}\,. \end{cases} \tag{42}$$

D. Ac Voltage Support

The priority of the GSC is to regulate dc-link voltage. If $|i^{\star}_{qf}| < I_{f,\mathrm{mx}}$, there is some room to steer $i^{\star}_{df}$ as to support DFIG stator voltage magnitude. To this end, the command $i^{\star}_{df}$ for (32) originates from a one-axis anti-windup PI controller:

$$i^{*}_{df} = k_{\mathsf{pi}v}\left(\sqrt{\frac{2}{3}}v_V v_\omega V^{\star}_s - \widehat{v}_{qs}\right) + z_{dv} \tag{43}$$

$$\frac{d}{dt}z_{dv} = \frac{1}{\tau_{\mathsf{pi}v}}(-z_{dv} + i^{\star}_{df}) \tag{44}$$

$$i^{\star}_{df} = \mathscr{L}\left(i^{*}_{df}, -i_{df,\mathrm{mx}}, i_{df,\mathrm{mx}}\right) \tag{45}$$

$$i_{df,\mathrm{mx}} = \sqrt{I^2_{f,\mathrm{mx}} - (i^{\star}_{qf})^2}\,. \tag{46}$$

The command $V^{\star}_s$ is the one used in (14) whereas v_V, v_ω are defined in (15). Please, note that the variables v_V and v_ω are not considered in present literature to control the GSC in DFIG-based systems [17], [20]. These are deemed important to prevent high volts-per-hertz values during restoration if frequency declines [30]. The filtered stator voltage magnitude $\widehat{v}_{qs}$ is from (19). The saturation function $\mathscr{L}$ is defined in (42).

The limit $i_{df,\mathrm{mx}}$ in (46) depends on $i^{\star}_{qf}$ of (40) to prioritize dc-link voltage regulation which is critical for RSC controllability [46, p. 485]. It is instructive to clarify that $i^{\star}_{qf}$ (40) and $i^{\star}_{df}$ (45) both belong to an origin-centered circle of radius $I_{f,\mathrm{mx}}$ which prevents violation of GSC current limits.

TABLE III
PARAMETERS OF A 2-MW DFIG WIND TURBINE SYSTEM

Par.	Val.	Unit	Par.	Val.	Unit	Par.	Val.	Unit
ρ	1.225	kg/m^3	R_w	55	m	P	6	-
C	50	mF	r_b	2	Ω	J_m	130	kg·m^2
L_M	1.526	mH	L_{ls}	0.09	mH	L'_{lr}	0.145	mH
r_s	1.4	mΩ	r'_r	0.992	mΩ	f_{sw}	3	kHz
G	118.5128	-	J_w	4.2	Mkg·m^2	N_{rs}	1	-
$\lambda^{\star}$	8.1	-	β_{mn}	0	Deg	β_{mx}	35	Deg
C_f	1	mF	L_f	0.36	mH	r_f	6.8	mΩ

Rated grid voltage $V^{\star}_s = 690$ Vrms at 60 Hz.
Rated dc-link voltage $v^{\star}_{dc} = 2$ kV.
Braking resistor activation threshold $v^{\dagger}_{dc} = 2.15$ kV.
Rated electrical output power $P_{\mathrm{e,mx}} = 2.0$ MW.

TABLE IV
TYPE 3 WIND TURBINE BLACKSTART CONTROLLER PARAMETERS

Par.	Val.	Unit	Par.	Val.	Unit	Par.	Val.	Unit
$k_{\mathsf{pi}r}$	0.289	V/A	$\tau_{\mathsf{pi}r}$	2	ms	τ_{vx}	10	μs
$k_{\mathsf{pi}s}$	0.6	A/V	$\tau_{\mathsf{pi}s}$	20	ms	τ_{ix}	10	μs
$V^{\star}_s$	690	Vrms	τ_v	5.3	ms	τ_s	5.3	ms
τ_g	10.6	ms	k_ω	0.05	p.u.	τ_e	5.3	ms
$k_{\mathsf{pi}f}$	0.7132	V/A	$\tau_{\mathsf{pi}f}$	2	ms	$I_{r,\mathrm{mx}}$	3.0	kA
$k_{\mathsf{pi}c}$	0.1183	A/J	$\tau_{\mathsf{pi}c}$	40	ms	$I_{s,\mathrm{mx}}$	2.0	kA
$k_{\mathsf{pi}v}$	0.6	A/V	$\tau_{\mathsf{pi}v}$	20	ms	$I_{f,\mathrm{mx}}$	1.0	kA
k_V	0.02	p.u.	$k_{\mathrm{V/Hz}}$	1.05	p.u.	τ_E	0.1	s
$f^{\star}_S$	60	Hz	ω_b	120π	rad/s	$\omega^{\star}_{\mathsf{e}}$	120π	rad/s
ω^{*}_m	163	rad/s	$E^{\star}_{dc}$	0.1	MJ			

V. CASE STUDY

Two case studies are developed to show the performance of the notional wind-dominant power system of Fig. 3 during recovery from a blackout. In case study I, the turbines are steered by the blackstart control systems in Sections III and IV following the procedure in Section II which are the major novelties in this paper. In case study II, we contrast the performance of the proposed grid-forming strategy against the one in [26]. In both case studies, three turbines like the one in Fig. 1 are challenged to energize transmission cables, electric motors, unbalanced and electronic loads. They are also confronted to

TABLE V
TIMED CIRCUIT BREAKERS EVENTS

	C1	C2	C3	C9	C10	C4	C5	C11	C12	C6	C8	C7
$t_c(s)$	2.5	2.6	2.7	3.0	3.5	4.0	4.0	4.5	5.0	9.0	15.0	20.0
$t_o(s)$	-	-	-	-	-	-	-	-	-	-	-	20.5

ride through a line-to-line fault during restoration. Each k-th wind turbine ($k \in \{1, 2, 3\}$) has a 2-MW/690-V DFIG.

A. Case I: Simulation Setup

A detailed simulation model of Fig. 3 was implemented in PLECS [51]. The simulation was conducted on a server equipped with two AMD EPYC 7742 CPUs running at 3.5 GHz. The CPU time of one core to simulate $T = 35$ s of reality was 2.3 hours ca. The RSCs of the three turbines—WT1, WT2, and WT3—switch at 3.0 kHz. The GSC of WT1 in Fig. 1 also switches at 3.0 kHz. The GSCs of WT2 and WT3 are implemented using average-value models to reduce simulation time. The simulation parameters are listed in Table III and IV. Each 0.69/13.2-kV 2.5–MVA step-up transformer in Fig. 3 has 5% impedance. The two transmission cables use a distributed parameter representation [52].

The insulated-gate bipolar transistors (IGBT) and diodes of the RSC and GSC correspond to the ABB HiPak IGBT Module 5SNA3600E170300 and 5SNA1600E170100 [53], respectively. Their upper-limit junction operating temperature is 150°C. To test the fault ride through capability, a line-to-line fault between phases 'a' and 'b' is applied as shown in Fig. 3 for $t \in [20, 20.5]$. A line-to-line fault is considered because this class of disturbances can trigger widespread disconnection of converter-based resources [54]–[56]. The wind speed profiles of each k-th turbine $v_{w,k}$ ($k \in \{1, 2, 3\}$) are reported in Fig. 8. They are 80-meter observations at the National Renewable Energy Laboratory's Flatirons Campus [30].

The simulation results are reported in Figs. 6–12. They capture the response to restoration events by respectively closing or opening the circuit breakers C1–C12 of Fig. 3 at times t_c and t_o, q.v. Table V. To simplify the reporting process, the study illustrates, for example, per-unit stator voltage $\breve{V}_{s,1}$, stator current $\breve{I}_{s,1}$, rotor current $\breve{I}_{r,1}$, and GSC current $\breve{I}_{f,1}$ magnitudes with respect to the turbine ratings. They are calculated from *qd* variables via (3). The variables in Figs. 1–3 are defined in Table II. Figure 10 reports relative speed $\Delta\omega_{\mathrm{e},k} = \omega_{\mathrm{e},k} - (\omega_{\mathrm{e},1} + \omega_{\mathrm{e},2} + \omega_{\mathrm{e},3})/3$ for $k = 1, 2, 3$ to ascertain synchronism.

The initial conditions of the system in Fig. 3 are: (i) all circuit breakers C1–C12 are open, (ii) the RSC and GSC of each turbine are turned off, (ii) the step-up transformers, transmission cables, and loads are de-energized, (iii) the rotor speed of each DFIG is spinning at $\omega_m = 163$ rad/s, (iv) the initial dc-link voltage $v_{dc,k} = 0.1$ kV for all k, and (v) the surrounding temperature of the RSC and GSC is 25°C.

B. Case I: Restoration Performance of Wind Turbines

The electrical, thermal, and mechanical responses of the Type 3 wind turbines are reported in Figs. 6–8. Figure 6 shows the electrical and thermal response of WT1. The dynamic responses of WT2 and WT3 are similar to WT1. The learnings

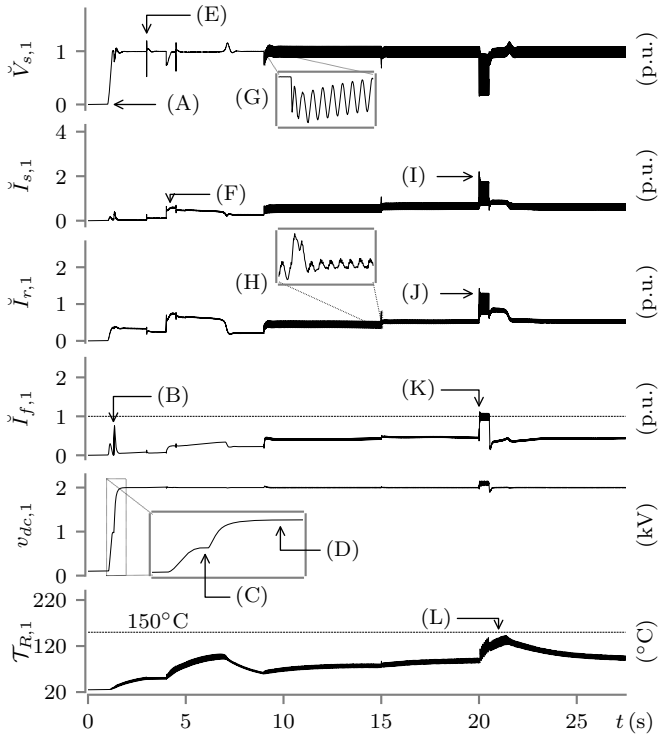

Fig. 6. Case I: Magnitudes of stator voltage, stator current, rotor current, GSC current as well as dc-link voltage and RSC temperature of WT1 for $t \in [0, 27]$ s.

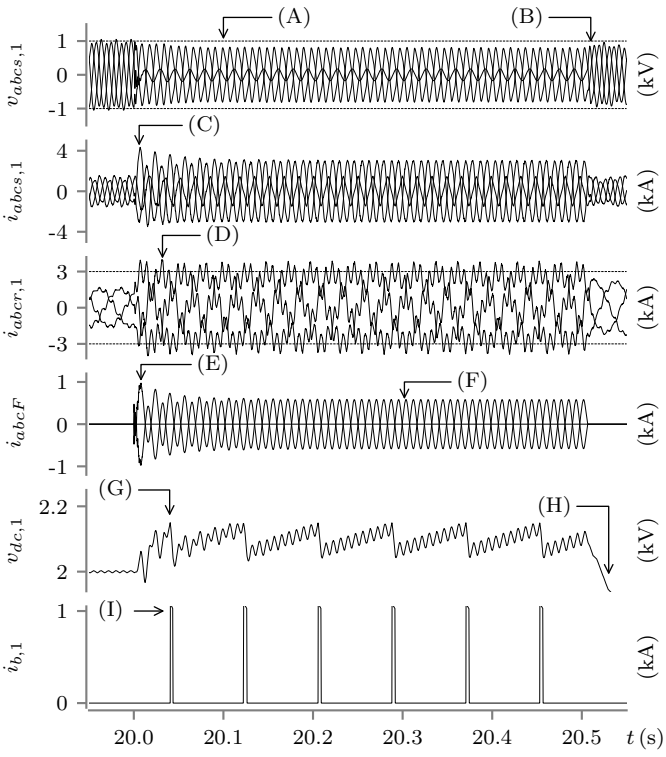

Fig. 7. Case I: Line-to-line stator voltages and currents; rotor currents; fault currents; dc-link voltage and braking-resistor current from WT1 for $t \in [20, 20.5]$ s.

from Fig. 6 are: (A) The DFIG unit is commanded to independently blackstart at $t = 1$ s, hence, $\breve{V}_{s,1} : 0 \to 1$ p.u. (B) The GSC current magnitude is 0.75 p.u. by $t = 1.3$ s because the GSC charges the dc-link capacitor. (C) $v_{dc,1}$ rises from 0.1 kV

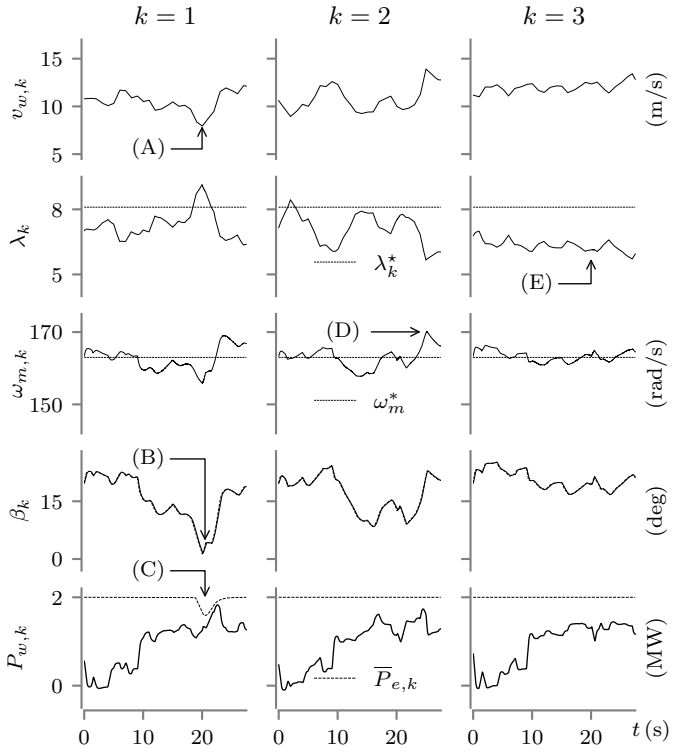

Fig. 8. Case I: Wind speed, tip speed ratio, DFIG rotor speed, pitch angle, and aerodynamic power of each k-th turbine for $t \in [0, 27]$ s.

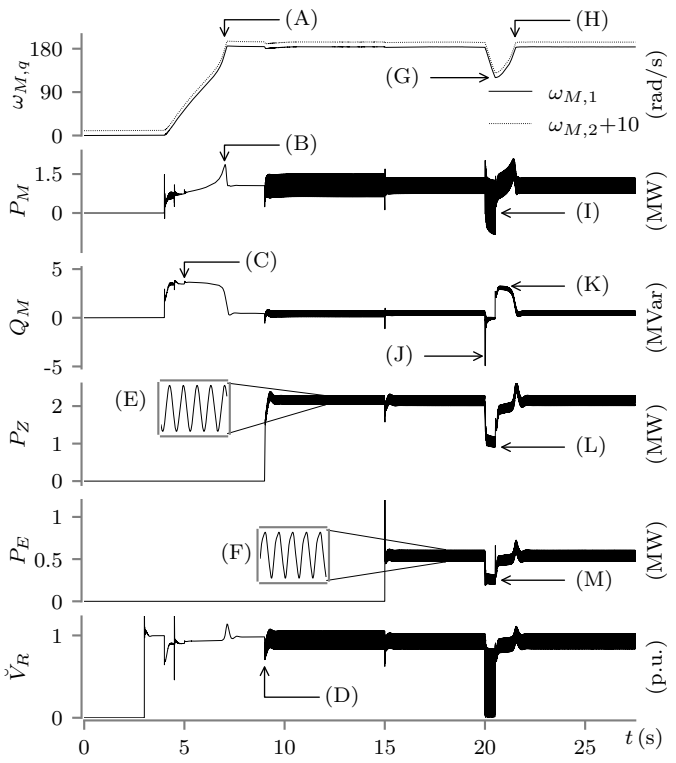

Fig. 9. Case I: Load responses for $t \in [0, 27]$ s.

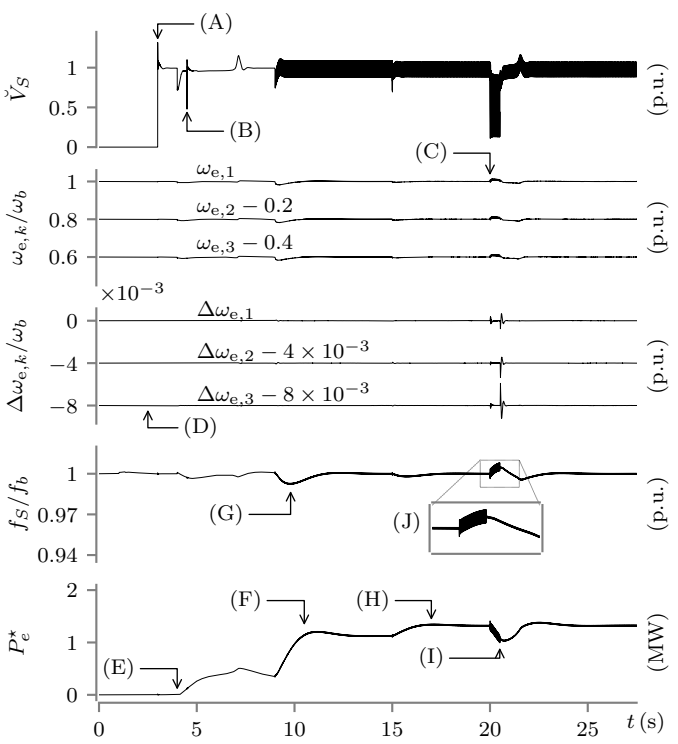

Fig. 10. Case I: PCC voltage magnitude, converter reference frame speed, relative speed, system frequency and turbine power set point for $t \in [0, 27]$ s.

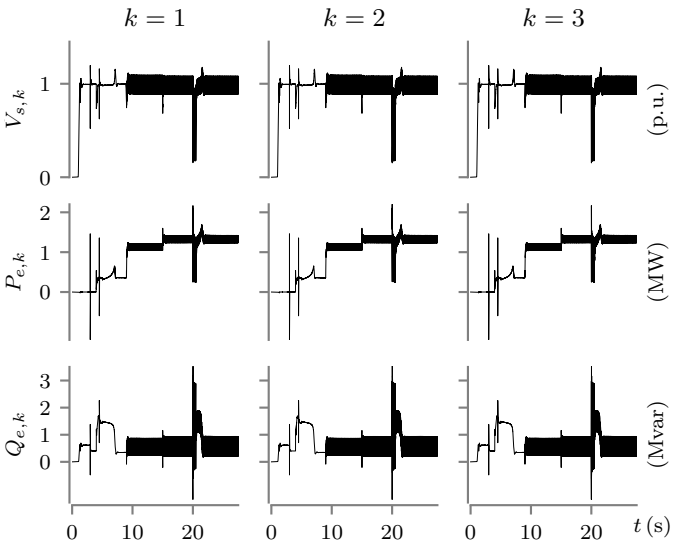

Fig. 11. Case I: Voltage magnitude and active/reactive power measured at the low-voltage transformer side of each k-th turbine for $t \in [0, 27]$ s.

to 0.9 kV c.a. because the GSC in off state rectifies stator voltages. (D) The GSC controller is turned on by $t = 1.3$ s to steer $v_{dc,1}$ from 0.9 to 2.0 kV. The PCC in Fig. 3 is energized with WT1 at $t = 2.5$ s by closing C1. The other turbines WT2 and WT3 synchronize to WT1 at $t = 2.6$ s and $t = 2.7$ s by closing C2 and C3, respectively, which completes the blackstart process. (E) The stator voltage magnitude $\breve{V}_{s,1}$ drops by $t = 3$ s to 0.52 p.u. and then rises to 1.19 p.u. because one transmission cable is energized by closing C9, it quickly settles at its rated value. A similar voltage dip and rise in $\breve{V}_{s,1}$ occurs by $t = 4.5$ s when energizing the second cable.

The impacts of energizing the loads on WT1 voltages and currents magnitudes are reported in Fig. 6. There: (F) $\breve{I}_{s,1}$ by $t = 4$ s is as high as 0.69 p.u. because the motor loads withdraw reactive power during start up. $\breve{I}_{s,1}$ drops to 0.11 p.u. when the motors reach rated speed by $t = 7$ s, q.v. $\omega_{M,q}$

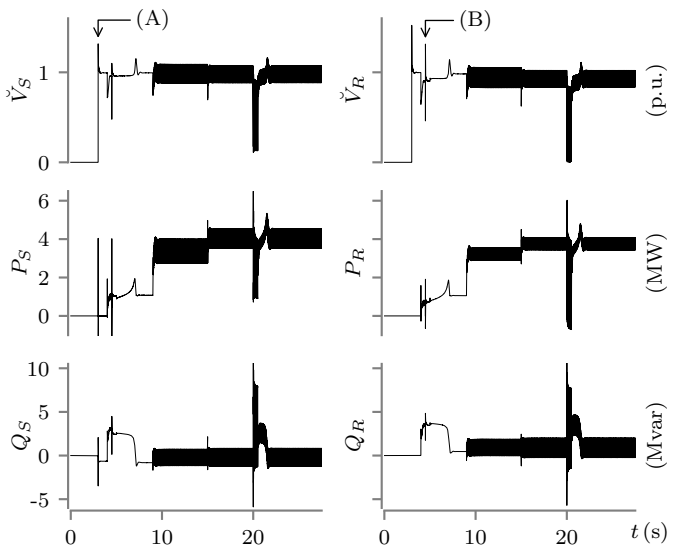

Fig. 12. Case I: Voltage magnitudes and active/reactive powers observed at the PCC and load feeder bus for $t \in [0, 27]$ s.

in Fig. 9. (G) $\breve{V}_{s,1}$ begins oscillating at 120 Hz ca. by $t = 9$ s when energizing the unbalanced load. (H) The impact of energizing the electronic load on $\breve{I}_{r,1}$ by $t = 15$ s is minor.

Now, this case study focus on the performance of the DFIG-based wind turbines during a line-to-line fault which is respectively applied and removed at $t = 20$ and $t = 20.5$ s, q.v. Fig. 3. Fig. 6 elucidates that: (I) $\breve{I}_{s,1}$ can be as high as 2.2 p.u. (J) $\breve{I}_{r,1}$ can be as high as 1.43 p.u. which violates rated limits. (K) $\breve{I}_{f,1}$ rises to 1.12 p.u. for voltage support, q.v. Section IV-D. (L) $\mathcal{T}_{R,1}$ reaches 143°C by $t = 21$ s which is below of the RSC thermal limit, 150°C, hence the semiconductor switches are intact.

Figure 7 reports select waveforms to ascertain the fault ride through capability of the WT1 from Fig. 3. It also reports the three-phase currents into the fault, i_{abcF}. The waveforms that pertain to WT2 and WT3 were similar, hence not depicted. In Fig. 7: (A) The line-to-line stator voltages, $v_{abs,1}$, $v_{bcs,1}$, and $v_{cas,1}$ are notoriously asymmetrical. The waveform of smallest magnitude is $v_{abs,1}$, q.v. Fig. 1. (B) Stator voltages recover to pre-fault conditions by $t = 20.5$ s when the fault is cleared. (C) The stator current $i_{as,1}$, q.v. Fig. 1 is as high as 4.33 kA. (D) The rotor current $i_{br,1}$ momentarily violates the considered limit $I_{r,\text{mx}} = 3.0$ kA. The RSC controller from Section III maintains the rotor currents around rated limits. Inspection of temperature $\mathcal{T}_{R,1}$ pointed by (L) in Fig. 6 after $t = 20$ s reveals that the this current trespassing is not problematic. (E) The magnitude of the fault current i_{aF} can be as high as 0.97 kA by $t = 20$ s. (F) The fault currents settle at 0.59 kA which are relatively low to activate over-current protection systems. (G) $v_{dc,1}$ is as high as 2.15 kV by $t = 20.04$ s, which leads to the activation of the BKR. In Fig. 1, the BKR activates if $v_{dc,1} \geq v_{dc}^{\dagger} = 2.15$ kV. (H) $v_{dc,1}$ drops to 1.9 p.u. when the fault is removed at $t = 20.5$ s, but it recovers to rated, q.v. Fig. 6. (I) The BKR current momentarily reaches 1 kA by $t = 20.04$ s; thus, the BKR is needed to ride through faults.

Figure 8 informs about the mechanical response of individual Type 3 wind turbines. In Fig. 8: (A) The wind speed, $v_{w,1}$, is as low as 7.9 m/s by $t = 20$ s which is coincident with the fault . (B) The pitch angle β_1, decreases to 1.6 deg because of (A). (C) The command $\overline{P}_{e,1}$ in Fig. 2 lowers to 1.59 MW so that the RSC controller lowers active power injection into the grid to prevent rotor stalling [30]. (D) The DFIG-rotor speed $\omega_{m,2}$ reaches 170 rad/s because of wind-speed increase. (E) The tip-speed ratio λ_3 does not fluctuate significantly because wind speed is almost steady.

C. Case I: Restoration Performance of Loads

This subsection focus on the dynamic performance of the motors as well as the unbalanced and electronic loads in Fig. 3. Figure 9 shows that: (A) The rotor speed of the motors $\omega_{M,q}$ $(q = 1, 2)$ accelerate from 0 to 184 rad/s ca. in 3 s. (B) P_M overshoots to 1.87 MW ca. by $t = 7.0$ s when reaching rated speed. (C) The reactive power, Q_M, during motor startup is as high as 3.81 MVar; Q_M rapidly declines by $t = 8$ s because the motors are reaching rated speed. (D) Voltage magnitude of the feeder, $\breve{V}_R$, q.v. v_{abcR} in Fig. 3 begins oscillating when the unbalanced load is energized by $t = 9$ s. (E) The active power P_Z (by the unbalanced load) oscillates between 2.0 and 2.3 MW at 120 Hz. (F) The power P_E (by the electronic load) fluctuates between 0.47 MW and 0.61 MW after $t = 15$ s. The impact of the unbalanced and electronic loads on the current and voltage waveforms of the WT1 are also shown in Fig. 7 for $t < 20$ s. There, the rotor currents $i_{abcr,1}$ and stator voltages $v_{abcs,1}$ are unbalanced and have some non-linear distortion.

During the fault, it is interesting to observe in Fig. 9 that: (G) The speed of the motors $\omega_{M,q}$ $(q = 1, 2)$ drops to 120 rad/s ca. by $t = 20.5$ s. (H) The speed of the motors recover to pre-fault values by $t = 22$ s. (I) P_M is distorted and oscillates around 0 MW. (J) Q_M is as low as -4.9 MVar by $t = 20$ s which means reactive power flows from the motors into the grid. (K) Q_M by $t = 20.5$ s is as high as 3.25 MVar to steer $\omega_{M,q}$ to rated values. (L) P_Z, q.v. Fig. 3, drops to 0.91 MW. (M) P_E, can be as low as 0.19 MW by $t = 20$ s. After the fault is cleared at $t = 20.5$ s, all the loads in Fig. 3 return to pre-fault operating conditions.

D. Case I: Overall Restoration Performance

The emphasis of this subsection is on the overall performance of the wind-dominant power system in Fig. 3. From Fig. 10, one can deduce that: (A) The PCC voltage magnitude $\breve{V}_S$ from v_{abS} and v_{cbS}, q.v. Fig. 3, is as high as 1.31 p.u. when one of the transmission cable is energized by $t = 3$ s; it quickly recovers to rated. (B) $\breve{V}_S$ fluctuates from 0.48 to 1.15 p.u. when the second transmission cable is energized by $t = 4.5$ s, it also swiftly returns to rated. (C) The speed $\omega_{\text{e},k}$ from (5) deviates from rated by $t = 20$ s because of the fault. (D) The wind turbines relative speed, $\Delta\omega_{\text{e},k}$, remains around zero when they synchronize by $t = 2.5$ s. (E) The power command, $P_e^{\star}$, from the frequency controller in Fig. 2 rises when the motors are energized by $t = 4$ s. (F) $P_e^{\star}$ is as high as 1.21 MW when the unbalanced load is energized by $t = 9$ s. This signifies that each turbine was

commanded to output 1.21 MW. (G) The system frequency, f_S, momentarily decreases from rated to 0.99 p.u. because of the unbalanced load energization. (H) $P_e^\star$ rises to 1.35 MW after the electronic load is energized by $t = 15$ s. (I) $P_e^\star$ is as low as 1.0 MW during the fault by $t = 20$ s because the wind turbines reject loads. (J) During the fault, f_S rises because the wind turbines reject loads. Because $\breve{V}_S$ and f_S remained close to rated values, there were no voltage and frequency regulation problems. Further, $\Delta\omega_{e,k}$ remained close to zero which is indicative of absence of synchronization problems.

This subsection also reports the voltage magnitudes as well as the active and reactive powers observed at different points in the grid. In particular, Fig. 11 shows $\breve{V}_{s,k}$, $P_{e,k}$, and $Q_{e,k}$, which are measured at the low voltage side of the step-up transformers of each k-th wind turbine, q.v. Fig. 3. Their responses are practically identical because they all employ the same control strategy and follow common voltage and speed set-points. The most notorious fluctuations in voltage and powers at $t = 20$ s are caused by the line-to-line fault.

Figure 12 depicts: (i) $\breve{V}_S$, P_S, and Q_S observed at the PCC as well as (ii) $\breve{V}_R$, P_R, and Q_R observed at the load feeder bus, q.v. Fig. 3. We clarify, for example, that P_S reflects the active power transmitted via the *two* cables in Fig. 3. The magnitude of $\breve{V}_S$ is slightly lower than $\breve{V}_{s,k}$ in Fig. 11 because of the voltage drop in the step-up transformers. The 1.32 p.u. and 1.31 p.u. over-voltages respectively pointed by (A) and (B) in Fig. 12 occur when the transmission lines are energized because of their capacitive nature. The power P_S *closely* matches the addition of $P_{e,k}$ for $k = 1, 2, 3$ in Fig. 11 at each point in time; 'closely' because of power losses in the transformers. The power oscillations observed in P_S and P_R are different because of the transmission line dynamics. Major spikes in Q_S and Q_R are observed during the motor start-up after $t = 4$ s, during the fault, and motor speed recovery by $t = 20.5$ s, i.e., after the fault is cleared.

The overall restoration process of the notional wind-dominant grid in Fig. 3 was successful. The motor, unbalanced, and power electronics loads were restored in 11 s ca.: the load restoration started at $t = 4$ s and ended by $t = 15$ s. The total blackstart and restoration time lasted 15 s after the DFIG rotor speed reached its set-point ω_m^*.

E. Case II: Comparative Study

In this subsection, the performance of the proposed grid-forming strategy in case study I is contrasted against [26]. The strategy in [26] employs rotor-flux oriented control, *proportional* stator voltage regulation, and a virtual-synchronous-machine law to generate the 'e' frame angle of Section II-D. The grid-forming control system in [26] does not employ current-limiting strategies to ride through faults and requires a PLL to synchronize the GSC to the DFIG-stator voltages. The restoration responses when using the control strategy in [26] are reported in Figs. 13, 14, 15, and 16. Next, they are compared with the ones in Figs. 6, 7, 9, and 10, respectively.

In Fig. 13: (A) The DFIG-stator voltage magnitude, $\breve{V}_{s,1}$ reaches 2.17 p.u. during startup which contrast the smooth voltage buildup in Fig. 6. (B) The DFIG stator voltage magnitude, $\breve{V}_{s,1}$ drops to 0.86 p.u. during motor startup which

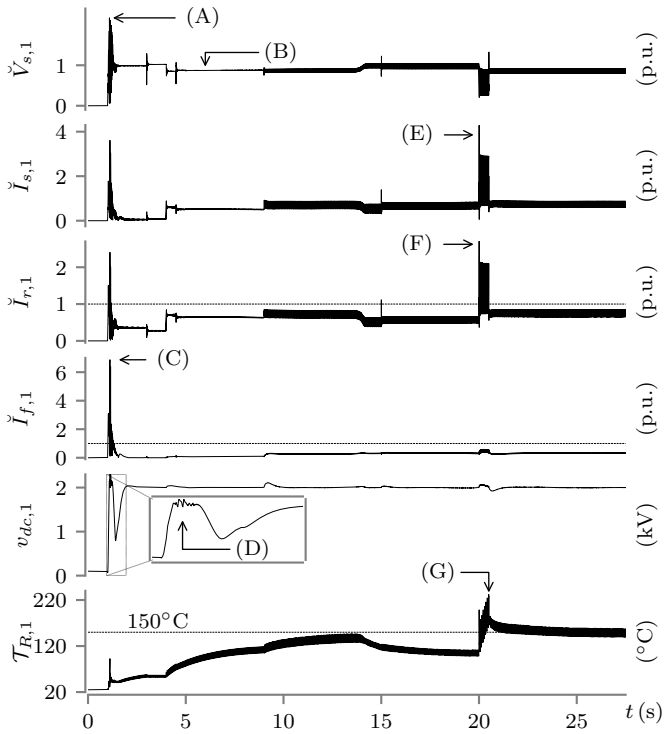

Fig. 13. Case II: Magnitudes of stator voltage, stator current, rotor current, GSC current, dc-link voltage as well as RSC temperature of WT1 equipped with blackstart controller in [26] for $t \in [0, 27]$ s.

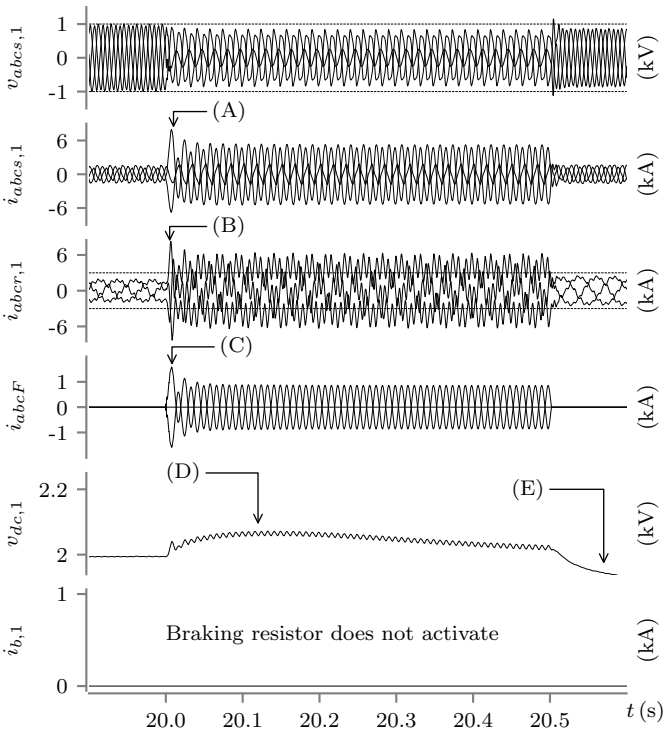

Fig. 14. Case II: Line-to-line stator voltages and currents; rotor currents; fault currents; and dc-link voltage when WT1 is equipped with the blackstart controller in [26] for $t \in [20, 20.5]$ s.

contrast the 0.97-p.u. voltage drop in Fig. 6 after $t = 4.0$ s. (C) The GSC current magnitude $\breve{I}_{f,1}$ raises to 6.87 p.u. of its rating during dc-link capacitor charging which contrast the 0.75 p.u. spike in Fig. 6. The $\breve{I}_{f,1}$ over-current is not observed

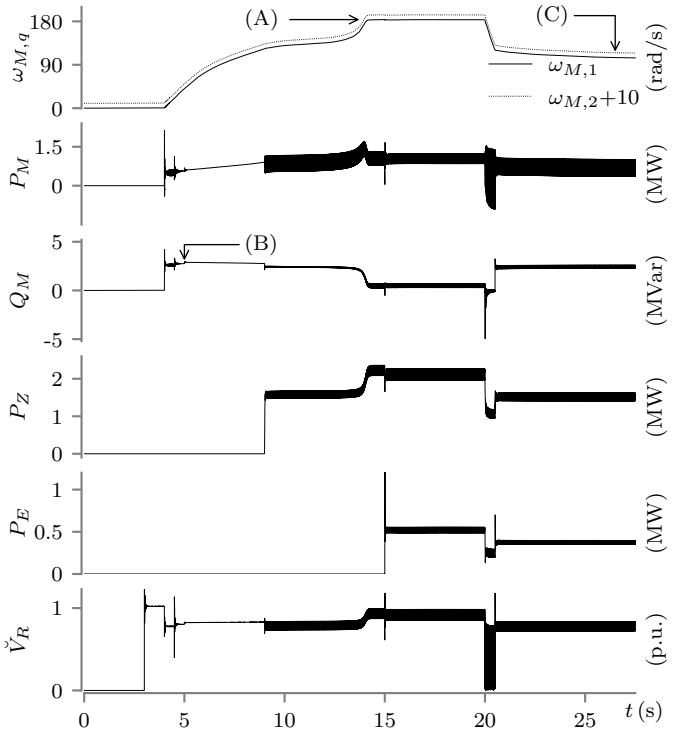

Fig. 15. Case II: Load responses when Type 3 wind turbines are equipped with the blackstart controller in [26] for $t \in [0, 27]$ s.

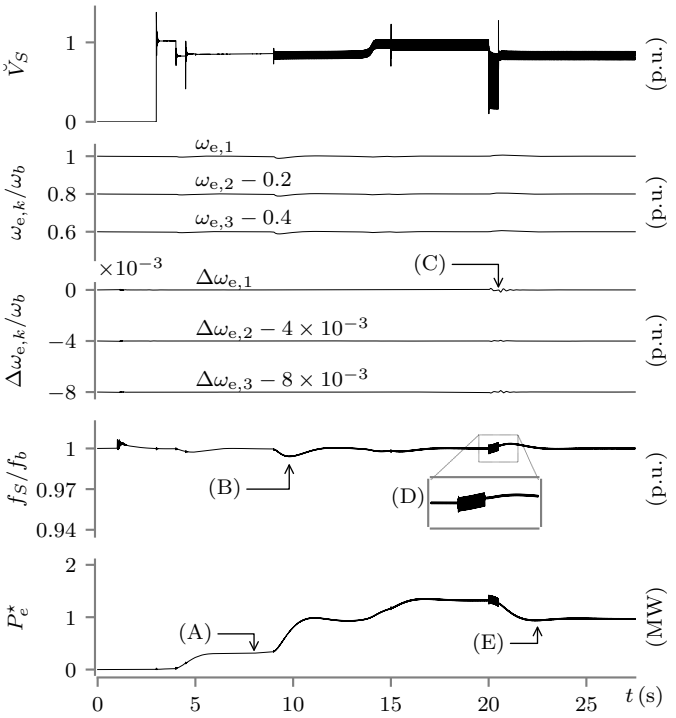

Fig. 16. Case II: PCC voltage magnitude, converter reference frame speed, relative speed, system frequency, and turbine power set point of WT1 equipped with blackstart controller in [26] for $t \in [0, 27]$ s.

in [26] because a battery bank is used to power the RSC during blackstart. (D) The dc-link voltage $v_{dc,1}$ reaches 2.15 kV and activates the breaking resistor because the RSC injects power into the dc-link which does not occur in Fig. 6. (E) During the line-to-line fault, the DFIG-stator current magnitude is as high as 4.28 p.u. whereas it only reaches 2.2 p.u. in Fig. 6. (F) The RSC peak current magnitude is as high as 2.91 p.u. of rated, but it is only as high as 1.43 p.u. in Fig. 6. (G) The RSC temperature, $\mathcal{T}_{R,1}$, is as high as 232°C which violates the RSC temperature rating, i.e., 150°C; in Fig. 6, the peak of $\mathcal{T}_{R,1}$ only reaches 143°C.

Figure 14 illustrates select waveforms during the line-to-line fault. These traces elucidate that: (A) The DFIG stator peak current is as high as 7.96 kA because the RSC current is not limited, but it only reaches 4.33 kA in Fig. 7. (B) The RSC peak current is as high as 8.30 kA while this peak is only as high as 4.0 kA Fig. 7. (C) The peak of the fault currents is as high as 1.59 kA which is physically unrealistic because the RSC thermal limits; this peak is only 0.97 kA in Fig. 7. (D) $v_{dc,1}$ is as high as 2.07 kV because the GSC is generating high ac currents for dc-link voltage regulation; it reaches 2.15 kV in Fig. 7. (E) $v_{dc,1}$ momentarily drops to 1.93 kV after the fault is cleared whereas it drops to 1.9 kV in Fig. 7 which is not a major difference.

Figure 15 informs the restoration performance of the loads in Fig. 3. One can infer that: (A) The direct-drive motors slowly reach rated speed by $t = 14$ s because the DFIG voltage is as low as 0.86 p.u.; they reach rated speed by $t = 7$ s in Fig. 9. (B) The reactive power Q_M during motor startup is only 2.94 MVar because of the voltage drop whereas it is as high as 3.81 MVar in Fig. 9. (C) After the fault is cleared, the motor speeds do not return to rated because of sustained low voltage $\check{V}_R$ which is not the case in Fig. 9.

Figure 16 illustrates the overall performance of the wind-dominant power system when using [26]. The learnings are: (A) The turbine set point $P_e^\star$ is as high as 0.34 MW by $t = 8.0$ s during motor startup because of low voltage, but $P_e^\star$ is as high as 0.52 MW in Fig. 10. (B) The system frequency f_S is as low as 0.99 p.u. which is comparable with the system frequency in Fig. 10. (C) During the line-to-line fault, the relative speed deviations, $\Delta\omega_{e,k}$ ($k = 1, 2, 3$), are smaller than the ones in Fig. 10 because a virtual-synchronous-machine law is used in [26]. (D) f_S oscillates during the line-to-line fault which is also observed in Fig. 10. (E) After the fault is cleared, $P_e^\star$ is as low as 0.93 MW which is significant lower than 1.32 MW which is observed in Fig. 10 after $t = 20.5$ s.

VI. Conclusion

This paper has set forth a grid-forming control system for DFIG-based turbines so that they can restore power systems while withstanding recovery transients. Further, the Type 3 topology with this control system can ride through symmetrical and asymmetrical faults, q.v. Sections III and IV. To achieve this challenging goal, we leveraged a new class of two-axis anti-windup proportional-integral (PI) regulators that can bound two-axis DFIG rotor current commands within ratings [30]. We also devised a set of feedforward control loops to mitigate the impacts of restoration transients on grid-forming operation.

We demonstrated in Section V that the turbines can energize two transmission branches, direct-drive motors, as well as unbalanced and electronic loads. Our contributions were

benchmarked against a recent grid-forming strategy [26] which exhibits voltage regulation problems during motor acceleration and lacks of current-limiting techniques to withstand faults. In this paper, the Type 3 turbines can ride through line-to-line faults that last 30 cycles of 60 Hz. Remarkably, NERC recently reported the disconnection of converter-based resources during line-to-line faults that have been recently reported [55], [56]; hence, this paper is timely. The Type 3 turbines are also capable of withstanding low wind speed events as in [30], cooperating with Type 4 assets, following changes in voltage and frequency set-points, as well as riding through three-phase and single line-to-ground faults, albeit these features were not reported here. Overall, this paper is useful towards securing blackstart resources [1], [3], [13], satisfying NERC standards for resilience to blackouts and reliability to faults [34], [40], and addressing the third grand challenge of wind energy [42].

Future work will consist of: (i) Comparing the resilience value of wind, solar, and battery resources to blackouts which is a complex task [57]. (ii) Assessing EMT simulations of the blackstart and restoration processes of large power systems which requires special simulation acceleration techniques [58]. And (iii) conducting MW experimentation which is critical for field deployment of the advances herein.

APPENDIX

A. Reference Frame Transformations

For control, we extensively use specialty reference frame transformations [46, p. 111]. In particular, we transform and filter line-to-line voltages v_{abx} and v_{cbx} into qd quantities:

$$\frac{d}{dt}[v^{\nu}_{qx}, v^{\nu}_{dx}]^{\top} = \frac{1}{\tau_{vx}}(-[v^{\nu}_{qx}, v^{\nu}_{dx}]^{\top} + K_v(\theta_\nu)[v_{abx}, v_{cbx}]^{\top}) \tag{47}$$

where τ_{vx} is a time constant for the first order filter and:

$$K_v(\theta_\nu) = \frac{2}{3}\begin{bmatrix}\cos\theta_\nu & \cos(\theta_\nu + 2\pi/3)\\ \sin\theta_\nu & \sin(\theta_\nu + 2\pi/3)\end{bmatrix}. \tag{48}$$

The indicator $\nu \in \{\mathsf{e}, \mathsf{s}, \mathsf{c}\}$ differentiates qd-variables arising from: (i) a synchronous angle θ_{e}, (ii) a relative angle $\theta_{\mathsf{s}} = \theta_{\mathsf{e}} - \theta_{\mathsf{r}}$ [46, p. 222], and (iii) a GSC angle θ_{c}.

Similarly, the following transformation [46, p. 112]:

$$K_i(\theta_\nu) = \frac{2}{\sqrt{3}}\begin{bmatrix}\cos(\theta_\nu - \pi/6) & \sin(\theta_\nu)\\ \sin(\theta_\nu - \pi/6) & -\cos(\theta_\nu)\end{bmatrix} \tag{49}$$

is used to convert line currents, i_{ax} and i_{bx}, into qd-axis ones:

$$\frac{d}{dt}[i^{\nu}_{qx}, i^{\nu}_{dx}]^{\top} = \frac{1}{\tau_{ix}}(-[i^{\nu}_{qx}, i^{\nu}_{dx}]^{\top} + K_i(\theta_\nu)[i_{ax}, i_{bx}]^{\top}) \tag{50}$$

where τ_{ix} is a time constant to filter current ripples.

The ESTM set-points $v^{\star}_{abc\chi} = [v^{\star}_{a\chi}, v^{\star}_{b\chi}, v^{\star}_{c\chi}]^{\top}$ ($\chi \in \{r, f\}$) are mapped from qd commands $v^{\star}_{q\chi}$ and $v^{\star}_{d\chi}$ as follows:

$$[v^{\star}_{a\chi}, v^{\star}_{b\chi}, v^{\star}_{c\chi}]^{\top} = T^{\top}(\theta_\nu)[v^{\star}_{q\chi}, v^{\star}_{d\chi}]^{\top} \tag{51}$$

$$T(\theta_\nu) = \begin{bmatrix}\cos(\theta_\nu) & \cos(\theta_\nu - 2\pi/3) & \cos(\theta_\nu + 2\pi/3)\\ \sin(\theta_\nu) & \sin(\theta_\nu - 2\pi/3) & \sin(\theta_\nu + 2\pi/3)\end{bmatrix}. \tag{52}$$

B. Tuning of RSC Control Parameters

Let τ_{str} be the settling of the RSC current regulator:

$$k_{\mathsf{pir}} = \frac{10L'_{lr}}{\tau_{\mathsf{str}}} - r'_r \text{ and } \tau_{\mathsf{pir}} = \frac{k_{\mathsf{pir}}}{L'_{lr}}\left(\frac{\tau_{\mathsf{str}}}{5}\right)^2. \tag{53}$$

Also, let τ_{sts} be the settling of the DFIG voltage regulator:

$$k_{\mathsf{pis}} = \frac{30C_f}{\tau_{\mathsf{sts}}} \text{ and } \tau_{\mathsf{pis}} = 0.4\tau_{\mathsf{sts}}. \tag{54}$$

In this paper $\tau_{\mathsf{str}} = 10\,\text{ms}$ and $\tau_{\mathsf{sts}} = 5\tau_{\mathsf{str}}$.

ACKNOWLEDGEMENT

We thank Dr. Vahan Gevorgian, Chief Engineer at the National Renewable Energy Laboratory, for his insightful technical discussions. We also thank the anonymous Referees for their comments and suggestions to improve this paper.

REFERENCES

[1] "FERC-NERC-regional entity joint review of restoration and recovery plans: Blackstart resources availability," FERC and NERC, Tech. Rep., May 2018.
[2] J. R. Gracia *et al.*, "Hydropower plants as black start resources," Oak Ridge Nat. Lab., Tech. Rep. ORNL/SPR-2018/1077, May 2019.
[3] J. G. O'Brien *et al.*, "Electric grid blackstart: Trends, challenges, and opportunities," Pacific Northwest Nat. Lab., Tech. Rep. PNNL-29118, May 2021.
[4] R. Bowers and C. Owen, "The United States installed more wind turbine capacity in 2020 than in any other year," eia.gov. https://www.eia.gov/todayinenergy/detail.php?id=46976#:~:text=According%20to%20data%20recently%20published,13.2%20GW%20added%20in%202012., (accessed Nov. 16, 2021).
[5] AEMO, "Application of advanced grid-scale inverters in the NEM," Australian Energy Market Operator, Tech. Rep., Aug. 2021.
[6] "Statement of the North American Electric Reliability Corporation," in *2021 Annu. Rel. Tech. Conf.*, Sep. 2021. [Online]. Available: https://www.ferc.gov/media/nerc-panel1
[7] J. Halliday, "Rhode Island natural gas outage," U.S. Dept. of Transp., Tech. Rep. 164488, Aug. 2019.
[8] C. King, J. Rhodes, and J. Zarnikau, "The timeline and events of the February 2021 Texas electric grid blackouts," The Univ. of Texas at Austin, Tech. Rep., Jul. 2021.
[9] J. Glisan, "Iowa monthly weather summary-January 2021," Iowa Dept. of Agriculture and Land Stewardship, Tech. Rep., May 2021.
[10] Annual 2020 climate summary and highlights. Weather Forecast Office.
[11] U.S. Energy Information Administration, "Electricity data browser," [Online]. Available: https://www.eia.gov/electricity/, (accessed Nov. 16, 2021).
[12] K. Reynolds, "Request for Presidential disaster declaration," Aug. 2020.
[13] H. Jain, G.-S. Seo, E. Lockhart, V. Gevorgian, and B. Kroposki, "Blackstart of power grids with inverter-based resources," in *2020 IEEE Power & Energy Soc. General Meeting*, Montreal, Canada, Aug. 2–6 2020, pp. 1–5.
[14] B. Hoen, J. Diffendorfer, J. Rand, L. Kramer, C. Garrity, and H. Hunt, "United States wind turbine database," January 21, 2022. doi:10.5066/F7TX3DN0.
[15] N. Pogaku, M. Prodanovic, and T. C. Green, "Modeling, analysis and testing of autonomous operation of an inverter-based microgrid," *IEEE Trans. Power Electron.*, vol. 22, no. 2, pp. 613–625, Mar. 2007.
[16] G. Iwanski and W. Koczara, "DFIG-based power generation system with UPS function for variable-speed applications," *IEEE Trans. Ind. Electron.*, vol. 55, no. 8, pp. 3047–3054, Aug. 2008.
[17] V.-T. Phan and H.-H. Lee, "Performance enhancement of stand-alone DFIG systems with control of rotor and load side converters using resonant controllers," *IEEE Trans. Ind. Appl.*, vol. 48, no. 1, pp. 199–210, Jan. 2012.
[18] R. Cardenas, R. Pena, S. Alepuz, and G. Asher, "Overview of control systems for the operation of DFIGs in wind energy applications," *IEEE Trans. Ind. Electron.*, vol. 60, no. 7, pp. 2776–2798, Jul. 2013.

[19] A. B. Ataji, Y. Miura, T. Ise, and H. Tanaka, "Direct voltage control with slip angle estimation to extend the range of supported asymmetric loads for stand-alone DFIG," *IEEE Trans. Power Electron.*, vol. 31, no. 2, pp. 1015–1025, Feb. 2016.

[20] N. K. Swami Naidu and B. Singh, "Experimental implementation of doubly fed induction generator-based standalone wind energy conversion system," *IEEE Trans. Ind. Appl.*, vol. 52, no. 4, pp. 3332–3339, Jul. 2016.

[21] L. Sun, C. Peng, J. Hu, and Y. Hou, "Application of type 3 wind turbines for system restoration," *IEEE Trans. Power Syst.*, vol. 33, no. 3, pp. 3040–3051, May 2018.

[22] W. Du, R. H. Lasseter, and A. S. Khalsa, "Survivability of autonomous microgrid during overload events," *IEEE Trans. Smart Grid*, vol. 10, no. 4, pp. 3515–3524, Jul. 2019.

[23] M. Rostami, S. M. Madani, and S. Ademi, "Sensorless closed-loop voltage and frequency control of stand-alone DFIGs introducing direct flux-vector control," *IEEE Trans. Ind. Electron.*, vol. 67, no. 7, pp. 6078–6088, Jul. 2020.

[24] S. Puchalapalli and B. Singh, "A single input variable FLC for DFIG-based WPGS in standalone mode," *IEEE Trans. Sustain. Energy*, vol. 11, no. 2, pp. 595–607, Apr. 2020.

[25] S. Shah and V. Gevorgian, "Control, operation, and stability characteristics of grid-forming type III wind turbines," in *19th Wind Integration Workshop*, Nov. 11–12, 2020.

[26] J. L. Rodríguez-Amenedo, S. A. Gómez, J. C. Martínez, and J. Alonso-Martinez, "Black-start capability of DFIG wind turbines through a grid-forming control based on the rotor flux orientation," *IEEE Access*, vol. 9, pp. 142 910–142 924, Oct. 2021.

[27] J. D. Watson, Y. Ojo, K. Laib, and I. Lestas, "A scalable control design for grid-forming inverters in microgrids," *IEEE Trans. Smart Grid*, vol. 12, no. 6, pp. 4726–4739, Nov. 2021.

[28] M. Chen, D. Zhou, A. Tayyebi, E. Prieto-Araujo, F. Dörfler, and F. Blaabjerg, "Generalized multivariable grid-forming control design for power converters," *IEEE Trans. Smart Grid*, vol. 13, no. 4, pp. 2873–2885, Jul. 2022.

[29] Q. Hu, R. Han, X. Quan, Z. Wu, C. Tang, W. Li, and W. Wang, "Grid-forming inverter enabled virtual power plants with inertia support capability," *IEEE Trans. Smart Grid*, 2022, early access.

[30] H. N. Villegas Pico and V. Gevorgian, "Black-start capability and survivability of wind turbines with fully-rated converters," *IEEE Trans. Energy Convers.*, early access.

[31] J. Morren and S. de Haan, "Ridethrough of wind turbines with doubly-fed induction generator during a voltage dip," *IEEE Trans. Energy Convers.*, vol. 20, no. 2, pp. 435–441, Jun. 2005.

[32] P.-H. Huang, M. S. El Moursi, W. Xiao, and J. L. Kirtley Jr, "Novel fault ride-through configuration and transient management scheme for doubly fed induction generator," *IEEE Trans. Energy Convers.*, vol. 28, no. 1, pp. 86–94, Mar. 2013.

[33] H. N. Villegas Pico and D. C. Aliprantis, "Voltage ride-through capability verification of DFIG-based wind turbines using reachability analysis," *IEEE Trans. Energy Convers.*, vol. 31, no. 4, pp. 1387–1398, Dec. 2016.

[34] *Frequency and Voltage Protection Settings for Generating Resources*, NERC PRC-024-3, Jul. 2020.

[35] Y. Lin *et al.*, "Research roadmap on grid-forming inverters," Nat. Renewable Energy Lab., Tech. Rep., Nov. 2020.

[36] "Solar future study," U.S. Dept. of Energy, Tech. Rep., Sep. 2021.

[37] P. W. Sauer, M. A. Pai, and J. H. Chow, *Power system dynamics and stability: with synchrophasor measurement and power system toolbox*. John Wiley & Sons, 2017.

[38] T. Ackermann, *Wind power in power systems*. Hoboken, NJ: Wiley, 2005.

[39] "North American energy resilience model," U.S. Dept. of Energy, Washington DC, Tech. Rep., Jul. 2019.

[40] *System Restoration from Blackstart Resources*, NERC EOP-005-3, Jan. 2018.

[41] NERC, "2021 state of reliability," North American Reliability Corporation, Atlanta, GA, USA, Tech. Rep., Aug. 2021.

[42] P. Veers *et al.*, "Grand challenges in the science of wind energy," *Sci.*, vol. 366, no. 6464, pp. 1–9, Oct. 2019.

[43] M. Chandorkar, D. Divan, and R. Adapa, "Control of parallel connected inverters in standalone AC supply systems," *IEEE Trans. Ind. Appl.*, vol. 29, no. 1, pp. 136–143, Jan. 1993.

[44] B. Snyder, "Excitation selections," cat.com. https://www.cat.com/en_US/by-industry/electric-power/Articles/White-papers/excitation-selections.html, (accessed Jul. 31, 2021).

[45] J. Fortmann, S. Engelhardt, J. Kretschmann, C. Feltes, and I. Erlich, "New generic model of DFG-based wind turbines for RMS-type simulation," *IEEE Trans. Energy Convers.*, vol. 29, no. 1, pp. 110–118, Mar. 2014.

[46] P. Krause, O. Wasynczuk, S. D. Sudhoff, and S. Pekarek, *Analysis of Electric Machinery and Drive Systems*, 3rd ed., J. Anderson, Ed. Piscataway, NJ, USA: Wiley, 2013.

[47] *IEEE Guide for AC Generator Protection*, IEEE Std. C37.102-2006, Rev. C37.102-1995, Feb. 2007.

[48] *IEEE Standard for Interconnection and Interoperability of Inverter-Based Resources (IBRs) Interconnecting with Associated Transmission Electric Power Systems*, IEEE Std 2800-2022.

[49] K. Åström and T. Hägglund, *PID controllers, theory, design, and tuning*, 2nd ed. Research Triangle Park, NC: Instrum. Soc. America, 1995.

[50] S. Skogestad and I. Postlethwaite, *Multivariable feedback control: analysis and design*. Hoboken, NJ, USA: Wiley, 2007.

[51] *PLECS*, PLEXIM. Accessed: Aug. 02, 2022. [Online], Available: https://www.plexim.com/products/plecs.

[52] H. W. Dommel, "Digital computer solution of electromagnetic transients in single-and multiphase networks," *IEEE Trans. Power App. Syst.*, vol. PAS-88, no. 4, pp. 388–399, Apr. 1969.

[53] Hitachi ABB, "Insulated gate bipolar transistor (IGBT) and diode modules," hitachienergy.com. https://www.hitachienergy.com/us/en/offering/product-and-system/semiconductors/insulated-gate-bipolar-transistor-igbt-and-diode-modules, (accessed Oct. 20, 2021).

[54] NERC & WECC staff report, "1,200 MW fault induced solar photovoltaic resource interruption disturbance report," North American Electric Reliability Corporation, Atlanta, GA, Tech. Rep., Jun. 2017.

[55] North American Electric Reliability Corporation, "Multiple solar PV disturbances in CAISO," NERC, Atlanta, GA, USA, Tech. Rep., Apr. 2022.

[56] NERC, "Panhandle wind disturbance," North American Electric Reliability Corporation, Atlanta, GA, Tech. Rep., Aug. 2022.

[57] J. M. Miller, H. N. Villegas Pico, I. Dobson, A. Bernstein, and B. Cui, "Feedback control approaches for restoration of power grids from blackouts," *Electric Power Syst. Res.*, vol. 211, p. 108414, Jul. 2022.

[58] S. Subedi, M. Rauniyar, S. Ishaq, T. M. Hansen, R. Tonkoski, M. Shirazi, R. Wies, and P. Cicilio, "Review of methods to accelerate electromagnetic transient simulation of power systems," *IEEE Access*, vol. 9, pp. 89 714–89 731, Jun. 2021.

Hoang P. Dang (Student Member, IEEE) received the B.Sc. degree in electrical engineering from Iowa State University (ISU), Ames, IA, in 2021. At present, he is a graduate student in the electric power and energy systems group within the Department of Electrical and Computer Engineering at ISU.

His research interests include power system modeling, EMT simulation, and control; renewable energy integration; and power restoration processes.

Hugo N. Villegas Pico (Member, IEEE) earned the degree of Ingeniero en electrónica, automatización y control from Universidad de las Fuerzas Armadas - ESPE, Sangolquí, Ecuador, in 2008, the M.S. degree in electrical engineering from Iowa State University, Ames, IA, USA, in 2011, and the Ph.D. degree in electrical and computer engineering from Purdue University, West Lafayette, IN, USA, in 2016. He was a Fulbright scholar for 2009–2011.

Hugo was a Post-Doctoral Researcher of Power Engineering at the National Renewable Energy Laboratory, Golden, CO, USA for 2017–2019 and a Post-Doctoral Research Assistant at Purdue University, West Lafayette, IN, USA for 2016–2017. Hugo was also a Supervisor of electrical maintenance for CELEC EP Termopichincha, Ecuador, for 2007–2009. At present, Hugo is a Harpole-Pentair Assistant Professor in the Department of Electrical and Computer Engineering at Iowa State University. He also serves as an Associate Editor of IET Generation, Transmission & Distribution. Hugo's research interests lie at the intersection of renewable energy conversion, power system dynamics, power restoration processes, and control systems.